

Electroosmosis over charge-modulated surfaces with finite electrical double layer thicknesses: Asymptotic and numerical investigations

Uddipta Ghosh,^{1,2} Shubhadeep Mandal,¹ and Suman Chakraborty¹

¹*Indian Institute of Technology Kharagpur, Kharagpur 721302, West Bengal, India*

²*University of Rennes 1, CNRS Geosciences Rennes, UMR 6118, 35041 Rennes, France*

(Received 29 November 2016; published 20 June 2017)

Here we attempt to solve the fully coupled Poisson-Nernst-Planck-Navier-Stokes equations, to ascertain the influence of finite electric double layer (EDL) thickness on coupled charge and fluid dynamics over patterned charged surfaces. We go beyond the well-studied “weak-field” limit and obtain numerical solutions for a wide range of EDL thicknesses, applied electric field strengths, and the surface potentials. Asymptotic solutions to the coupled system are also derived using a combination of singular and regular perturbation, for thin EDLs and low surface potential, and good agreement between the two solutions is observed. Counterintuitively to common arguments, our analysis reveals that finite EDL thickness may either increase or decrease the “free-stream velocity” (equivalent to net throughput), depending on the strength of the applied electric field. We also unveil a critical EDL thickness for which the effect of finite EDL thickness on the free-stream velocity is the most prominent. Finally, we demonstrate that increasing the surface potential and the applied field tends to influence the overall flow patterns in the contrasting manners. These results may be of profound importance in developing a comprehensive theoretical basis for designing electro-osmotically actuated microfluidic mixtures.

DOI: [10.1103/PhysRevFluids.2.064203](https://doi.org/10.1103/PhysRevFluids.2.064203)

I. INTRODUCTION

Electroosmotic flows (EOFs) are central to the understanding of micro-hydrodynamics under the broad realm of electrokinetics [1–4], with applications in energy conversion [5,6] and subsurface flows [7,8], as well as in lab-on-a-chip–based devices for medical diagnostics [9,10]. Although a large number of studies [2,11–14] have been executed to address several aspects of electrokinetic motion in narrow confinements, most of these offer a relatively simplified model of an otherwise complicated and nonlinear phenomenon. Following the pioneering work of Ajdari [15], many researchers [16–21] have demonstrated that the presence of axial modulations in the surface charge can lead to various interesting flow patterns, which can be potentially used for mixing purposes in an otherwise low Reynolds number paradigm [17,22,23]. Patterned surface potentials also play important roles in applications like AC-electroosmosis [24–26], electrothermal flow actuation [27], and induced-charge electroosmosis [28,29] as well as thin-film patterning [30,31]. Many of these investigations make an *a priori* approximation that the ionic species concentrations within the electrical double layer (EDL) follow the Boltzmann distribution [1,32,33], which again undermines the intricate coupling between the ionic transport and fluid flow.

Recently, inspired by the seminal work of Saville [2], several studies, most notably those of Yariv and co-workers [29,34–37] along with many others [38–41], have addressed the said coupling between charge and momentum transport through the much celebrated Poisson-Nernst-Planck-Navier-Stokes (PNPNS) equations, albeit in the context of electrophoretic motion of small particles in the thin EDL limit. Recent studies on electrokinetic instabilities [42–44] have also accounted for ionic advection, which leads to a coupled modeling of electroosmotic transport. Although these studies were executed for large surface potentials, they did not consider presence of any background flow, while the “zeta potential” was considered to be uniform in nature. Only a handful of previous studies, most notably those of Zhao and co-workers [41,45] and Khair and Squires [39], have probed into the PNPNS equations to address the electrokinetic transport in the presence of charge modulated

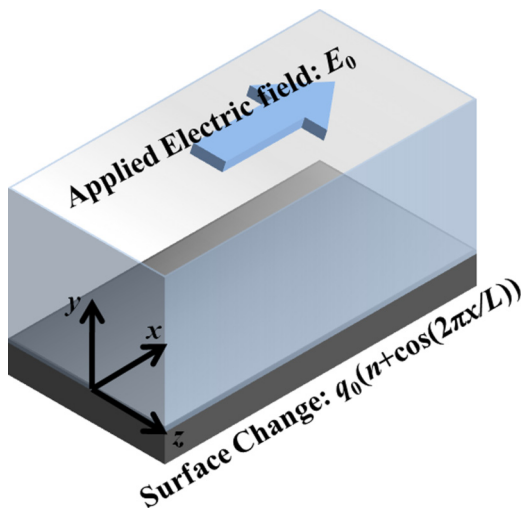


FIG. 1. Schematic of the physical system under consideration: an infinite body of liquid containing electrolytes resting on top of a solid surface bearing a modulated charge: $q_0[n + \cos(2\pi x'/L)]$. The origin is chosen to be on the wall; the x axis runs along the solid surface, while the y axis runs vertically upwards. An external steady electric field of magnitude E_0 is applied along the x axis to actuate the fluid motion.

surfaces. Zhao and co-workers addressed only the dynamics in the “weak field limit,” while their studies mostly focused on numerical methods without giving much insight into the charge and momentum transport through asymptotic analysis. On the other hand, Khair and Squires, while also exploring the dynamics in the weak field regime, mainly focused on concentration polarization in the bulk solution, without going into the details of the flow dynamics. Although the study of Khair and Squires gave valuable insights into the nature of salt concentration distribution through analytical (asymptotic) techniques, it nevertheless only evaluated the leading corrections as brought about by the externally applied field. Therefore, a close review of these and other relevant studies suggests that the general problem of electrokinetic flows over nonuniformly charged surfaces still has a lot of scope for development. More specifically, a combined investigation which addresses the intricate coupling between charge and momentum transport beyond the weak field limit, in the presence of nonuniformly charged surfaces, is yet to be carried out, to the best of our knowledge. Moreover, there also seems to be a relative dearth of studies which offer insight into the coupled charge and fluid dynamics by using analytical techniques, appropriately complemented by numerical solutions, highlighting the interesting physics in the process.

In light of the above, the present analysis focuses on the electroosmosis over charge-modulated surfaces, beyond the weak field limit. Our analysis can be divided into two parts. First, we solve the coupled PNPNS model numerically, accounting for a wide range of EDL thicknesses, applied electric field strength, and surface potentials, where none of these are asymptotically large. The second part consists of asymptotic solutions to PNPNS equations, in the thin EDL and low surface potential limit, while the field strength (defined precisely in the next section) is assumed to remain $O(1)$ in the process. To this end, a combination of singular and regular perturbation is employed to work out the corresponding asymptotic solutions. We subsequently compare the two solutions and show that reasonably good agreement can be observed between the two.

II. MODEL DESCRIPTION

A. Physical description of the system

Figure 1 shows a schematic representation of the system under consideration. It consists of a 1:1 electrolyte solution resting on top of a solid surface. The origin and the axis system have been shown

clearly in the schematic. The electrolyte concentration far away from the wall is c'_0 . The fluid has a viscosity of η and a dielectric constant ε . The solid surface bears a periodically modulated charge along the axial direction, given by $q'(x') = q_0[n + \cos(2\pi x'/L)]$. Consequently, the electrolytes gather around the solid wall to form an EDL. An external electric field of magnitude E_0 is applied along x axis (i.e., parallel to the solid surface) to actuate electroosmotic flow. The flow here is assumed to be steady and incompressible in nature.

Before moving towards the general formulation, at this stage it is important to discuss the relevant assumptions undertaken for the present analysis. First, we assume that the Reynolds number associated with the flow is low enough so that inertial effects can be neglected [46]. Second, in what follows, we would attempt to solve the relevant governing equations for a wide range of EDL thickness, applied field strength, and ‘‘surface charge.’’ However, we would strictly assume that the characteristic ‘‘zeta potential’’ as well as the strength of the applied electric field is not asymptotically large. Third, we would neglect all end effects in the axial direction. This would enable us to assume that the relevant variables remain periodic along the x axis. We reiterate that a number of previous studies [15,18] related to EOF have taken such an assumption. Fourth, in addition, the usual assumptions of the Poisson-Nernst-Planck model, i.e., point charges, noninteracting ions, etc. [47], are also invoked in this study.

B. Governing equations

We begin with a brief depiction of the dimensionless forms of the PNPNS equations relevant to the present work. Towards this, the characteristic length scale is chosen as $x_c = y_c = d$, where $d = L/2\pi$; the characteristic potential is the thermal scale, i.e., $\psi_c = kT/e$; the ionic species concentration scale is taken as $c_c \sim c'_0$; and the characteristic velocity is chosen as $u_c \sim \varepsilon k^2 T^2 / \eta d e^2$. Accordingly, the following nondimensional equations are obtained:

$$\psi = \varphi + \varphi_{\text{ext}} = \varphi - \beta x, \quad (1)$$

$$\text{Pe } \mathbf{v} \cdot \nabla c = \nabla^2 c + \nabla \cdot (\rho \nabla \varphi) - \beta \frac{\partial \rho}{\partial x}, \quad (2)$$

$$\text{Pe } \mathbf{v} \cdot \nabla \rho = \nabla^2 \rho + \nabla \cdot (c \nabla \varphi) - \beta \frac{\partial c}{\partial x}, \quad (3)$$

$$\delta^2 \nabla^2 \varphi = -\rho/2, \quad (4)$$

$$-\nabla p + \nabla^2 \mathbf{v} + \nabla^2 \varphi (\nabla \varphi - \beta \mathbf{e}_x) = 0, \quad \text{and } \nabla \cdot \mathbf{v} = 0. \quad (5)$$

The above equations have been represented in terms of net charge density, $\rho = c_1 - c_2$ and total salt concentration, $c = c_1 + c_2$. In Eq. (1), the total potential ψ has been decomposed [18] into the contribution from the external field ($\varphi_{\text{ext}} = -\beta x$) and that from the diffuse charges (φ). A number of very important nondimensional numbers appear in the above equations. These are as follows: (1) the applied field strength, $\beta = E_0 e d / kT$; (2) the Peclet number, signifying the ionic advection strength, $\text{Pe} = u_c d / D = \varepsilon k^2 T^2 / e^2 \eta D$; and (3) the nondimensional EDL thickness, $\delta = \lambda_D / d$, where $\lambda_D = \sqrt{\frac{\varepsilon k T}{2 c'_0 e^2}}$. The above equations are subject to the following boundary conditions:

$$\frac{\partial c}{\partial y} + \rho \frac{\partial \varphi}{\partial y} = 0; \quad \frac{\partial \rho}{\partial y} + c \frac{\partial \varphi}{\partial y} = 0; \quad \frac{\partial \varphi}{\partial y} = -\bar{\zeta}_0 \left(\frac{n + \cos x}{\delta} \right); \quad u = v = 0, \quad \text{at } y = 0, \quad (6)$$

$$\varphi \rightarrow 0, \quad \rho \rightarrow 0, \quad c \rightarrow 2, \quad v \rightarrow 0, \quad \text{and } \frac{\partial u}{\partial y} \rightarrow 0, \quad \text{as } y \rightarrow \infty. \quad (7)$$

As already mentioned, along the axial direction, all the variables are assumed to be periodic in nature. Note that another very important parameter appears in the boundary condition for potential at the wall, namely, in Eq. (6), defined as $\bar{\zeta}_0 = e q_0 \lambda_D / \varepsilon k T$. This parameter indicates the magnitude of

the characteristic EDL potential, with respect to the thermal potential. Usually, $\bar{\zeta}_0 \sim O(1)$ for EOFs, although the limit of low surface potential, defined by $\bar{\zeta}_0 \ll 1$, has also been analyzed in the literature [15,18,48]. On the other hand, Dukhin [49] and more recently others [29,50,51] have analyzed the high surface potential case, which implies $\bar{\zeta}_0 \gg 1$. Note that the above nondimensionalization has been carried out following the work of Saville [2].

In Eqs. (1)–(7), externally controllable parameters are β, δ , and $\bar{\zeta}_0$, while Saville [2] has shown that the ionic Peclet number (Pe) largely remains close to 0.5 for most ionic species in electric-field-driven phenomena, taking water as the liquid medium. In addition to this, since Pe mostly depends on fluid properties, it is rather difficult to alter Pe externally. In regard to the parameter δ , the most practically relevant scenario for EOF is the thin EDL limit [26,52], defined as $\delta \ll 1$, while a thick EDL is usually characterized by $\delta \sim O(1)$. In this regard, it should be noted that previous studies [49,50] have quantified asymptotically large applied field strength and surface charge density as $\beta, e^{|\bar{\zeta}_0|/2} \sim O(\delta^{-1}) \gg 1$, in the thin EDL limit. Additionally, the limit of $1 \ll \beta \ll \delta^{-1}$ also leads to a separate distinguished strong field limit. As already noted, here we stick to the cases of $\beta \sim O(1)$. The thin EDL limit has been rigorously addressed later in this work.

Equations (1)–(5), subject to the conditions (6) and (7), complete the mathematical description of the system under consideration. In the forthcoming sections, we proceed towards solving the said system of equations to deduce numerical as well as asymptotic solutions.

III. NUMERICAL SOLUTIONS

A majority of the previous investigations on EOFs, which have taken into account the fully coupled model [35], have mostly investigated the thin EDL limit only, which permits a singular asymptotic method based solution, taking δ as the gauge function. Other studies [41], which have considered relatively thicker EDLs, have done so only in the weak field regime, characterized by $\beta \ll 1$. Therefore, the aim of this section is to construct numerical solutions to Eqs. (1)–(5), subject to (6) and (7) for a wide range of foresaid parameters. To this end, we would assume all of β, δ , and $\bar{\zeta}_0$ to be arbitrary in nature, without being too large (as already described earlier), while the Peclet number Pe is taken to be strictly $O(1)$.

The numerical simulations were executed in a finite element [53] based commercial software package, COMSOL Multiphysics 4.4. The system of discretized algebraic equations have been solved using a Damped Newton method [54]. An in-built Multifrontal Massively Parallel Sparse direct linear solver [55,56] has been used to solve the discretized set of equations. In the present study, we have set the relative tolerance at 0.001. The details of computational domain and grid distribution are given in Appendix A.

One quantity of particular interest to us regarding the flow dynamics is the “free-stream velocity,” given by $\lim_{y \rightarrow \infty} u = u_\infty$. We can evaluate the free-stream velocity in the following way (based on the fact that the flow variables are periodic along the axial direction):

$$u_\infty = \frac{1}{2\pi} \int_0^{2\pi} u(y = H, x) dx. \quad (8)$$

While discussing the results, we would also focus on another quantity derived from u_∞ , defined as

$$\Delta u_\infty = u_\infty - u_{\infty, \delta=0}. \quad (9)$$

It can be easily inferred that the quantity Δu_∞ denotes the effect of finite EDL thickness (accounting for the coupling between momentum and charge transport) on the free-stream velocity. In other words, it is precisely the difference between the free-stream velocity, evaluated based on the full PNPNS model, and the one evaluated based on a Smoluchowski Slip velocity [15] approach. Note that the free-stream velocity here is analogous to the volume flow rate for equivalent flow through a confined channel. It is also important to note that, from a numerical point of view, the situation

$\delta = 0$ is not solvable, since it refers to an actual singular scenario. However, from analytical point of view, $u_{\infty, \delta=0}$ is evaluated simply from the Smoluchowski slip velocity [57] condition. Therefore, when evaluating (9) from numerical solutions, we would define $u_{\infty, \delta=0}$ as follows [57]:

$$u_{\infty, \delta=0} = -\beta\zeta(x). \quad (10)$$

In Eq. (10), $\zeta(x)$ is the ‘‘zeta potential’’ of the surface. In the present problem, it can be defined as follows [57]:

$$\zeta(x) = \frac{2kT}{e} \sinh^{-1} \left[\frac{eq(x)\lambda_D}{2\epsilon kT} \right], \quad \text{where } q(x) = \bar{\zeta}_0[n + \cos(x)]. \quad (11)$$

IV. ASYMPTOTIC SOLUTIONS FOR THIN EDL ($\delta \ll 1$)

A. Outline of the solution

Asymptotic solutions to thin EDL limit (defined as $\delta \ll 1$) require the application of singular perturbation [58,59]. Indeed, a number of previous studies [35,36,57,60] have applied matched asymptotic expansion to resolve the dynamics within the EDL, in the thin EDL limit. Assuming that the quantities $\bar{\zeta}_0$, β are not asymptotically large, a singular perturbation-based approach requires dividing the flow domain into two subdomains, with two distinct characteristic length scales. The first one is the EDL (the ‘‘inner layer’’), which has a characteristic length scale (in the y direction) of δ and lies just adjacent to the wall. Therefore, we need to rescale all the variables in accordance with the change in the length scale, while analyzing the dynamics within this layer. The second layer is the bulk (the ‘‘outer layer’’), which basically characterizes the zone outside the EDL. In this zone the length scales are all $O(1)$, which indicates that here all the variables scale as per the nondimensionalization scheme outlined at the beginning of Sec. II B and therefore require no further rescaling. At the edge of the EDL, we must asymptotically match all the outer variables with their counterparts in the inner layer. Finally, we note that for thin EDL limit the outer and the inner layer variables can be expanded in an asymptotic series of δ as follows:

$$\mathfrak{S} = \mathfrak{S}_0 + \delta\mathfrak{S}_1 + \delta^2\mathfrak{S}_2 + \dots \quad (12)$$

In Eq. (12), \mathfrak{S} can represent variables like u , v , p , etc. It is well known [57] that in the leading order of δ , the coupled charge and momentum transport problem has exact solutions for any kind of surface charge (or, equivalently zeta potential) distribution, even if $\bar{\zeta}_0 \sim O(1)$. However, as we move into higher order in δ (as we intend to do here), the resulting governing equations do not remain analytically tractable, for periodically patterned surface charge distribution. Therefore, in order to derive analytical solutions it is essential to assume the surface charge to be low enough, i.e., $\bar{\zeta}_0 \ll 1$. This allows us to further expand the relevant variables in an asymptotic series of $\bar{\zeta}_0$. Note that the said limit of low surface charge has been extensively used in Refs. [15,18,39,61] and is the key element in the famous Debye-Huckel linearization. Fortunately, $\bar{\zeta}_0 \ll 1$ leads to a regular asymptotic limit, wherein the variables in both the layers at every successive order of δ need to be expanded in a series of $\bar{\zeta}_0$ as follows:

$$\mathfrak{S}_k = \sum_{i=0}^{\infty} \bar{\zeta}_0^i \mathfrak{S}_k^{(i)}. \quad (13)$$

In Eq. (13), the subscript k denotes the k th order term in the series (12). Therefore, in essence, an analytical solution to the present problem necessitates application of a double asymptotic series, which is a combination of singular (in δ) and regular (in $\bar{\zeta}_0$) perturbation. In this regard, it is important to note that double perturbation series in fluid dynamics has been employed by a number of previous studies [46,60,62]. In the present analysis, we would determine only the first two terms having nonzero contribution to the velocity in the regular perturbation series of $\bar{\zeta}_0$, at every successive order of δ .

B. Outer layer equations

The outer layer equations are given by (2)–(5), subject to (7), which are the original nondimensional equations and the far field boundary conditions. These equations cannot satisfy the conditions (6) at the wall because of the presence of the “inner layer.” We reiterate that all the outer layer variables have to be expanded in an asymptotic series of δ , as mentioned in (12). We further note that in the limit of low surface potential ($\bar{\zeta}_0 \ll 1$), these variables have to be further rescaled to account for the low magnitude of the surface charge. These rescaled variables can be subsequently expanded in another regular asymptotic series of $\bar{\zeta}_0$, as shown in (13). The details of the rescaling and the solutions have been given in the forthcoming sections.

C. Inner layer equations

The variables are rescaled as follows in the inner layer [57]: $u \rightarrow U$; $v \rightarrow \delta V$; $p \rightarrow \delta^{-2} P$; $\varphi \rightarrow \Phi$; $\rho \rightarrow \Pi$; $c \rightarrow C$, while the length scales are rescaled as $x \rightarrow X$; $y \rightarrow \delta Y$. Enforcing the said rescaled variables in (2)–(5), we can derive the full set of inner layer equations. We would only explicitly mention these equations here for once and will refer to this section, when discussing the solutions at various orders of δ . The inner layer equations are given by

$$\frac{\partial^2 C}{\partial Y^2} + \frac{\partial}{\partial Y} \left(\Pi \frac{\partial \Phi}{\partial Y} \right) = \delta^2 \left[\text{Pe} \left(U \frac{\partial C}{\partial X} + V \frac{\partial C}{\partial Y} \right) - \frac{\partial}{\partial X} \left(\Pi \frac{\partial \Phi}{\partial X} \right) - \frac{\partial^2 C}{\partial X^2} + \beta \frac{\partial \Pi}{\partial X} \right], \quad (14)$$

$$\frac{\partial^2 \Pi}{\partial Y^2} + \frac{\partial}{\partial Y} \left(C \frac{\partial \Phi}{\partial Y} \right) = \delta^2 \left[\text{Pe} \left(U \frac{\partial \Pi}{\partial X} + V \frac{\partial \Pi}{\partial Y} \right) - \frac{\partial}{\partial X} \left(C \frac{\partial \Phi}{\partial X} \right) - \frac{\partial^2 \Pi}{\partial X^2} + \beta \frac{\partial C}{\partial X} \right], \quad (15)$$

$$\frac{\partial^2 \Phi}{\partial Y^2} + \frac{1}{2} \Pi = -\delta^2 \frac{\partial^2 \Phi}{\partial X^2}, \quad (16)$$

$$\frac{\partial^2 \Phi}{\partial Y^2} \frac{\partial \Phi}{\partial Y} - \frac{\partial P}{\partial Y} = \delta^2 \left[-\frac{\partial^2 V}{\partial Y^2} - \frac{\partial \Phi}{\partial X} \frac{\partial^2 \Phi}{\partial X^2} - \delta^2 \frac{\partial^2 V}{\partial X^2} \right], \quad (17)$$

$$\frac{\partial^2 U}{\partial Y^2} + \frac{\partial^2 \Phi}{\partial Y^2} \left(\frac{\partial \Phi}{\partial X} - \beta \right) - \frac{\partial P}{\partial X} = \delta^2 \left[-\frac{\partial^2 U}{\partial X^2} - \frac{\partial^2 \Phi}{\partial X^2} \left(\frac{\partial \Phi}{\partial X} - \beta \right) \right], \quad (18)$$

$$\frac{\partial U}{\partial X} + \frac{\partial V}{\partial Y} = 0. \quad (19)$$

These are subject to the following boundary conditions:

$$\text{at } Y = 0, \quad \frac{\partial C}{\partial Y} + \Pi \frac{\partial \Phi}{\partial Y} = 0; \quad \frac{\partial \Pi}{\partial Y} + C \frac{\partial \Phi}{\partial Y} = 0; \quad \frac{\partial \Phi}{\partial Y} = -\bar{\zeta}_0(n + \cos X); \quad U = V = 0. \quad (20)$$

The matching conditions at the edge of the EDL are given by [58]

$$\begin{aligned} \lim_{Y \rightarrow \infty} \Pi &= \lim_{y \rightarrow 0} \rho; & \lim_{Y \rightarrow \infty} \Phi &= \lim_{y \rightarrow 0} \varphi; & \lim_{Y \rightarrow \infty} C &= \lim_{y \rightarrow 0} c \\ \lim_{Y \rightarrow \infty} U &= \lim_{y \rightarrow 0} u; & \lim_{Y \rightarrow \infty} \delta V &= \lim_{y \rightarrow 0} v; & \lim_{Y \rightarrow \infty} \frac{1}{\delta^2} P &= \lim_{y \rightarrow 0} p. \end{aligned} \quad (21)$$

These variables have to be further expanded in an asymptotic series of δ , as shown in (12), while the matching has to be carried out at every successive order of δ . In the limit of low surface potential, i.e., when $\bar{\zeta}_0 \ll 1$, we would have to further rescale the inner layer variables (as mentioned in Sec. IV B) and expand the subsequent rescaled variables in a regular series of $\bar{\zeta}_0$, as delineated in (13). The details of rescaling and solutions have been demonstrated in the forthcoming sections.

Finally, we note that the matching criteria in (21) along with the boundary conditions are not enough to determine the unique solution to the problem. To this end, an additional pair of matching

conditions are required, namely, current and salt flux balance at the edge of the EDL [35,57]. These two additional conditions are the subject of the next subsection.

D. Charge and salt flux balance

The charge and salt flux balance can be carried out by directly matching the fluxes of the said quantities at the edge of the EDL. To this end, we first work out the proper scales for the charge and salt fluxes in the two layers. In the outer layer, the charge (\mathbf{i}) and salt (\mathbf{j}) fluxes are given by

$$\mathbf{i} = \text{Pe}v\rho - \nabla\rho - c(\nabla\varphi - \beta\mathbf{e}_x) \quad \text{and} \quad \mathbf{j} = \text{Pe}vc - \nabla c - \rho(\nabla\varphi - \beta\mathbf{e}_x). \quad (22)$$

In the inner layer, the fluxes have to be rescaled as follows: $i_x = I_x$; $i_y = \delta^{-1}I_y$, while similar scaling for the salt fluxes also holds true. Here, i_k denotes flux along the k th direction. The charge and salt transport in the inner layer can thus be expressed as (keeping in mind the other rescaled variables in the inner layer, as already mentioned in Sec. IV C):

$$\frac{\partial I_y}{\partial Y} + \delta^2 \frac{\partial I_x}{\partial X} = 0 \quad \text{and} \quad \frac{\partial J_y}{\partial Y} + \delta^2 \frac{\partial J_x}{\partial X} = 0. \quad (23)$$

Note that, Eq. (23) is just the Nernst-Planck equations written in terms of the inner layer fluxes. The matching condition at the edge of the EDL can be expressed as [35]

$$\lim_{Y \rightarrow \infty} \delta^{-1} I_y = \lim_{y \rightarrow 0} i_y \quad \text{and} \quad \lim_{Y \rightarrow \infty} \delta^{-1} J_y = \lim_{y \rightarrow 0} j_y. \quad (24)$$

The quantities $\lim_{Y \rightarrow \infty} I_y$ and $\lim_{Y \rightarrow \infty} J_y$ can be evaluated from (23) in the following way:

$$\begin{aligned} \lim_{Y \rightarrow \infty} I_y &= -\delta^2 \int_0^\infty \frac{\partial I_x}{\partial X} dY = -\delta \frac{\partial}{\partial X} \int_0^\infty \left\{ \frac{\partial \Pi}{\partial X} - \text{Pe}U\Pi + C \left(\frac{\partial \Phi}{\partial X} - \beta \right) \right\} dY, \\ \lim_{Y \rightarrow \infty} J_y &= -\delta^2 \int_0^\infty \frac{\partial J_x}{\partial X} dY = -\delta \frac{\partial}{\partial X} \int_0^\infty \left\{ \frac{\partial C}{\partial X} - \text{Pe}UC + \Pi \left(\frac{\partial \Phi}{\partial X} - \beta \right) \right\} dY. \end{aligned} \quad (25)$$

In Eq. (25), the rescaled inner layer variables from Sec. IV C have been used to express the fluxes in integral form. Combining (22), (24), and (25), the salt and charge flux balance can be expressed as

$$\begin{aligned} \lim_{y \rightarrow 0} \left(\frac{\partial \rho}{\partial y} - \text{Pe}v\rho + c \frac{\partial \varphi}{\partial y} \right) &= -\delta \frac{\partial}{\partial X} \int_0^\infty \left\{ \frac{\partial \Pi}{\partial X} - \text{Pe}U\Pi + C \left(\frac{\partial \Phi}{\partial X} - \beta \right) \right\} dY \\ \lim_{y \rightarrow 0} \left(\frac{\partial c}{\partial y} - \text{Pe}vc + \rho \frac{\partial \varphi}{\partial y} \right) &= -\delta \frac{\partial}{\partial X} \int_0^\infty \left\{ \frac{\partial C}{\partial X} - \text{Pe}UC + \Pi \left(\frac{\partial \Phi}{\partial X} - \beta \right) \right\} dY. \end{aligned} \quad (26)$$

The above flux matching equations are very similar to the overall balance equations derived by Schnitzer and Yariv [35] in connection to electrophoresis. Additionally, Khair and Squires [39] have also used a similar approach (which essentially uses a depth averaged current) to balance charge and salt fluxes across the EDL. Several other studies [26,63,64] have also used similar flux-matching conditions to capture the dynamics within and outside the EDL in connection to AC electrokinetics. Equations (2)–(5) in the outer layer, (14)–(19) in the inner layer, subject to the boundary conditions (7) (far field), (20) (wall), and the matching conditions (21) and (26) complete the singular description of the full PNPNS system.

E. The leading order solutions in δ

We will derive the leading order solutions for low surface potentials ($\bar{\zeta}_0 \ll 1$), although, as already discussed such an assumption is not necessary at this order. However, as we move towards the higher orders in δ , the said approximation will be crucial for deriving analytical solutions. Here we would emphasize on the basic rescaling rules, before the regular asymptotic expansions in terms of $\bar{\zeta}_0$

has been applied. Note that a host of previous studies [18,65] on electroosmotic flows over charge modulated surfaces have assumed low surface charge so as to linearize the governing equations.

We have noted that assumption of low surface charge necessitates further rescaling. To this end, we observe that the inner layer variables (at any order of δ) have to be further rescaled as follows for $\bar{\zeta}_0 \ll 1$: $U_k \rightarrow \bar{\zeta}_0 \bar{U}_k$; $V_k \rightarrow \bar{\zeta}_0 \bar{V}_k$; $P_k \rightarrow \bar{\zeta}_0^m \bar{P}_k$; $\Phi \rightarrow \bar{\zeta}_0 \bar{\Phi}_k$; $\Pi_k \rightarrow \bar{\zeta}_0 \bar{\Pi}_k$; $C_0 \rightarrow \bar{C}$, where U_k, V_k, \dots are k th order terms in the asymptotic series represented in (12). The value of the constant m for pressure depends on the order of approximation in δ , while all other variables rescale in the same way at every order of δ . For the leading order solutions, $m = 2$ [based on Eq. (17)]. Likewise, the outer layer variables also have to be rescaled in the following way: $\mathbf{v}_k \rightarrow \bar{\zeta}_0 \bar{\mathbf{v}}_k$; $p_k \rightarrow \bar{\zeta}_0 \bar{p}_k$; $\varphi_k \rightarrow \bar{\zeta}_0 \bar{\varphi}_k$; $c_k \rightarrow \bar{c}_k$; $\rho_k \rightarrow \bar{\zeta}_0 \bar{\rho}_k$, where a similar notation has been used. Note that all the rescaled variables are represented with a ‘‘breve’’ overhead. In the rest of this section, we will use only these rescaled variables. These can be further expanded in a regular asymptotic series of $\bar{\zeta}_0$, as represented in (13). For instance, in the inner layer, the U velocity can be expanded as $\bar{U}_k = \bar{U}_k^{(0)} + \bar{\zeta}_0 \bar{U}_k^{(1)} + \bar{\zeta}_0^2 \bar{U}_k^{(2)} + \dots$, while the velocity in the outer layer can be expanded as $\bar{\mathbf{v}}_k = \bar{\mathbf{v}}_k^{(0)} + \bar{\zeta}_0 \bar{\mathbf{v}}_k^{(1)} + \bar{\zeta}_0^2 \bar{\mathbf{v}}_k^{(2)} + \dots$. The above rescaling essentially indicates that for low values of surface potential, velocities, and EDL potential as well as the charge density are linearly proportional to $\bar{\zeta}_0$, as a first approximation. This is quite obvious, since if the surface charge is zero (i.e., if $\bar{\zeta}_0 = 0$), we would expect the charge density, EDL potential and the velocities to vanish. However, because of the presence of electrolytes, the concentration would still be nonzero (actually it will just be $c = 2$ everywhere), which is why the concentration has not been rescaled. Another interesting aspect of the rescaling process is that the pressure behaves differently in the outer and the inner layers. This is simply because in the EDL, the pressure is governed by the electrostatic body forces, while in the outer layer it is governed by the viscous forces.

We now have to enforce the above rescaled variables into the governing equations discussed in Secs. IV B–IV D to deduce the dynamics for low surface potential. We can further enforce the associated expansion in terms of $\bar{\zeta}_0$ into these equations to derive the successive approximations at various orders of $\bar{\zeta}_0$. Note that this procedure has to be repeated at every order of δ to make progress along the matched asymptotic series.

1. The $O(1,1)$ solutions

Equations and the boundary conditions along with the matching conditions for the leading order variables can be easily deduced from Secs. IV B and IV C. It can be easily shown [57] that the leading order charge density, potential, and concentration in the outer layer are given by

$$\bar{\rho}_0^{(0)} = \bar{\varphi}_0^{(0)} = 0 \quad \text{and} \quad \bar{c}_2^{(0)} = 2. \quad (27)$$

The expressions in (27) indicates that in the leading order, the outer layer is free of charge, and it essentially behaves like an electro-neutral solution. In the inner layer, the corresponding solutions are as follows (based on the PNP equations in the inner layer and the matching conditions):

$$\bar{\Phi}_0^{(0)} = (n + \cos X)e^{-Y}; \quad \bar{\Pi}_0^{(0)} = -2\bar{\Phi}_0^{(0)} \quad \text{and} \quad \bar{C}_0^{(0)} = 2. \quad (28)$$

It can be easily inferred that (28) represents the linearized limit (Debye-Huckel limit) of the Boltzmann distribution of charge and concentration [66]. The X velocity can now be evaluated from the x -momentum equation in the inner layer [Eq. (18)] in the following way:

$$\bar{U}_0^{(0)} = -\beta(n + \cos X)(1 - e^{-Y}). \quad (29)$$

Note that while determining $\bar{U}_0^{(0)}$, we have used the fact that this quantity must remain finite at the edge of the EDL, i.e., as $Y \rightarrow \infty$. The leading order Y velocity can be evaluated by integrating

the continuity equation as follows:

$$\tilde{V}_0^{(0)} = -\beta \sin X(Y - 1 + e^{-Y}). \quad (30)$$

Applying the matching conditions (21) for the velocities, we can deduce the boundary conditions for the outer layer velocities. These conditions are given by

$$\lim_{y \rightarrow 0} \tilde{u}_0^{(0)} = \lim_{Y \rightarrow \infty} \tilde{U}_0^{(0)} = -\beta[n + \cos(x)] \text{ and } \lim_{y \rightarrow 0} \tilde{v}_0^{(0)} = 0. \quad (31)$$

Recalling that $\tilde{\varphi}_0^{(0)} = 0$, at the leading order the outer flow is governed by simple Stokes equations with the following solutions:

$$\tilde{\mathbf{v}}_0^{(0)} = \tilde{u}_{\infty,0}^{(0)} \mathbf{e}_x + \nabla \times (\tilde{S}_0^{(0)} \mathbf{e}_z); \quad \tilde{S}_0^{(0)} = -\beta y e^{-y} \cos(x) \quad \text{and } u_{\infty,\delta=0}. \quad (32)$$

In Eq. (32), S is the stream function. From (31), we can easily infer that the said boundary condition merely represents the Smoluchowski slip velocity at leading order [i.e. at $O(1,1)$]. In (32), $\tilde{u}_{\infty,0}^{(0)}$ is the “free-stream” velocity at leading order and only has a linear contribution from the axially invariant part of the surface charge.

2. The $O(1, \tilde{\xi}_0^2)$ solutions

It can be very easily verified that the $O(1, \tilde{\xi}_0)$ solutions, i.e., $O(\tilde{\xi}_0)$ contributions in the leading order of δ is identically zero for all the related (rescaled) variables. We can deduce the solutions at $O(1, \tilde{\xi}_0^2)$ in much the same way, as done at the previous order. The solutions for the charge density, potential, and concentration in the outer layer are

$$\tilde{\rho}_0^{(2)} = \tilde{\varphi}_0^{(2)} = \tilde{c}_0^{(2)} = 0. \quad (33)$$

The solutions to charge density, potential, and concentration in the inner layer are given by

$$\begin{aligned} \tilde{C}_0^{(2)} &= (\tilde{\Phi}_0^{(0)})^2; \quad \tilde{\Pi}_0^{(2)} = -[2\tilde{\Phi}_0^{(2)} + \frac{1}{3}(\tilde{\Phi}_0^{(0)})^3] \\ \tilde{\Phi}_0^{(2)} &= \frac{1}{16}(n + \cos X)^3(e^{-Y} - \frac{1}{3}e^{-3Y}) \end{aligned} \quad (34)$$

The pressure (leading order) can be evaluated from the Y -momentum equation and reads $\tilde{P}_0^{(0)} = \frac{1}{2}(\tilde{\Phi}_0^{(0)})^2$. The velocities in the inner layer at $O(1, \tilde{\xi}_0^2)$ have the following expression:

$$\begin{aligned} \tilde{U}_0^{(2)} &= -\frac{\beta}{24}(n + \cos X)^3 \left(1 - e^{-Y} - \frac{1}{3}e^{-3Y} \right) \\ \tilde{V}_0^{(2)} &= \frac{\beta}{192} \{ (4n^2 + 1) \sin X + 4n \sin 2X + \sin 3X \} [e^{-3Y} - 9e^{-Y} - 6Y + 8]. \end{aligned} \quad (35)$$

The boundary conditions for the outer layer velocities can be derived from the matching conditions and read

$$\begin{aligned} \lim_{y \rightarrow 0} \tilde{u}_0^{(2)} &= \frac{1}{48} \beta n (2n^2 + 3n) + \frac{1}{32} \beta (4n^2 + 1) \cos(x) + \frac{1}{16} \beta n \cos(2x) + \frac{\beta}{96} \cos(3x) \\ \lim_{y \rightarrow 0} \tilde{v}_0^{(2)} &= 0. \end{aligned} \quad (36)$$

At $O(\bar{\zeta}_0^2)$ the outer layer is again force-free and hence the fluid motion is governed by the Stokes equations. The velocities have the following solutions:

$$\begin{aligned}\tilde{\mathbf{v}}_0^{(2)} &= \tilde{u}_{\infty,0}^{(2)} \mathbf{e}_x + \nabla \times (\tilde{S}_0^{(2)} \mathbf{e}_z); \quad \tilde{u}_{\infty,0}^{(2)} = \frac{\beta}{48}(2n^3 + 3n); \\ \tilde{S}_0^{(2)} &= \frac{\beta}{8} \left(n^2 + \frac{1}{4} \right) y e^{-y} \cos(x) + \frac{1}{16} \beta n y e^{-2y} \cos(2x) + \frac{\beta}{96} y e^{-3y} \cos(3x).\end{aligned}\quad (37)$$

Note that the solutions at this order are just the first correction to the Smoluchowski-Slip velocity-based solutions, subject to Debye-Huckel linearization. One interesting point to note is that the $O(1, \bar{\zeta}_0^2)$ outer flow field also contributes to the net transport of fluid, far from the solid surface. This contribution is however, not linear in n , which signifies the axially invariant part of the surface charge. However, all the velocities in the leading order of δ are always linearly proportional to β . A look at the far field velocities indicate that the $O(1, \bar{\zeta}_0^2)$ contribution leads to a decrease in the free-stream velocity.

F. The $O(\delta)$ problem

We would describe the procedure to derive the $O(\delta)$ solutions in detail, since this same method can be followed to deduce the higher order solutions in δ . In the low potential limit, we would require rescaling the variables in both the layers, as mentioned at the beginning of Sec. IV E. Note that at $O(\delta)$, the scaling parameter m for pressure in the inner layer is again $m = 2$. The governing equations in both the layers at this order can be easily evaluated from the full-scale equations discussed in Secs. IV B–IV D and hence have not been explicitly mentioned here for brevity.

1. The $O(\delta, 1)$ solutions

We would begin with the charge and salt flux balance equations, i.e., Eqs. (26), expressed at $O(\delta)$. Application of the said balance equations yields $[\partial \tilde{c}_1^{(0)} / \partial y]_{y=0} = [\partial \tilde{\varphi}_1^{(0)} / \partial y]_{y=0} = 0$. The Poisson equation in the outer layer gives us, $\tilde{\rho}_1^{(0)} = 0$. These conditions, in conjunction with the outer layer equation for concentration, simply indicate $\tilde{c}_1^{(0)} = 0$. However, to deduce the $O(\delta, 1)$ outer layer potential, we would need to derive the $O(\delta, \bar{\zeta}_0)$ correction to the concentration [based on the charge transport equation, i.e., Eq. (3) in the outer layer]. The salt flux balance at this order can be simplified to the following form: $[\partial \tilde{c}_1^{(1)} / \partial y]_{y=0} = \frac{\partial}{\partial X} \int_0^\infty \beta \tilde{\Pi}_0^{(0)} dY = 2\beta \sin(x)$. Noting that the outer layer equation for salt transport at $O(\delta, \bar{\zeta}_0)$ has the form [from Eq. (2)], $\nabla^2 \tilde{c}_1^{(1)} = \text{Pe} \tilde{\mathbf{v}}_0^{(0)} \cdot \nabla \tilde{c}_1^{(0)} = 0$ (since $\tilde{c}_1^{(0)} = 0$), we can easily deduce that the solution for concentration at this order reads

$$\tilde{c}_1^{(1)} = -2\beta e^{-y} \sin(x). \quad (38)$$

The expression in (38) can be plugged into the charge transport equation in the bulk at $O(\delta, 1)$ to write $\nabla^2 \tilde{\varphi}_1^{(0)} = (\beta/2) \partial \tilde{c}_1^{(1)} / \partial x$. This equation can be easily solved subject to the far field condition for potential and the previously derived condition at the edge of the EDL to deduce

$$\tilde{\varphi}_1^{(0)} = \frac{1}{2} \beta^2 (1 + y) e^{-y} \cos(x). \quad (39)$$

We now move towards the inner layer solutions for potential and concentration. To this end, we note that the concentration at $O(\delta, 1)$ is simply $\tilde{C}_1^{(0)} = 0$. We can, however, solve the inner layer equation for salt concentration [Eq. (14)] at $O(\delta, \bar{\zeta}_0)$ subject to the matching condition for salt concentration in (21) and the no-salt flux condition at the wall [Eq. (20)] to deduce

$$\tilde{C}_1^{(1)} = -2\beta \sin X. \quad (40)$$

This can be plugged into Eq. (15) at $O(\delta, 1)$ to determine the charge density, subject to no-flux condition at the wall and matching condition for charge density at $Y \rightarrow \infty$. The resulting solution is simply $\tilde{\Pi}_1^{(0)} = \beta^2 \cos(X) - 2\tilde{\Phi}_1^{(0)}$. The potential can be determined from the Poisson's equation at $O(\delta, 1)$ [i.e., Eq. (16)], subject to $\partial\tilde{\Phi}_1^{(0)}/\partial Y = 0$ at $Y = 0$ and the matching condition for potential in (21). The solution reads

$$\tilde{\Phi}_1^{(0)} = \frac{1}{2}\beta^2 \cos X. \quad (41)$$

The solution (38) indicates that the first concentration polarization in the outer layer occurs at $O(\delta\bar{\zeta}_0)$. This polarization is proportional to the external field strength, which indicates that the primary driving force behind this is the externally applied electric field. We further note from (39) that this concentration polarization also induces an excess outer layer potential at $O(\delta)$. However, the EDL is actually charge free at this order (note that $\tilde{\Pi}_1^{(0)} = 0$), which naturally indicates that the potential does not vary across the EDL. Application of external electric field disturbs the equilibrium distribution of ions inside the EDL, which on the aggregate (i.e., when integrated across the entire EDL) violates the charge and salt conservation in the inner layer. Consequently the induced potential in the bulk drives a net current into (or, out of the) EDL so as to ensure overall conservation of charge and salt.

We can now solve the X -momentum equation in the inner layer at $O(\delta)$ to deduce the corresponding velocity. It turns out that this velocity is a simple shear flow of the form

$$\tilde{U}_1^{(0)} = 2\beta Y \cos X. \quad (42)$$

In fact the shear rate inside the EDL [i.e., the factor $2\beta \cos(X)$] can be determined by matching the inner layer velocity with its counterpart in the outer layer. The Y velocity in the inner layer can be determined by integrating the continuity equation as follows:

$$\tilde{V}_1^{(0)} = \beta Y^2 \sin X. \quad (43)$$

The boundary conditions for the outer layer velocities can be obtained using the matching conditions in (21), following the method outlined in Sec. IV E. However, at $O(\delta)$ the outer layer is acted upon by a force, originating from induced potential in the bulk, although the bulk remains charge free at this order. In fact, this particular force originates from concentration polarization and hence drives a chemio-osmotic flow in the bulk. The outer layer equation of motion is then given by $-\nabla\tilde{p}_1^{(0)} + \nabla^2\tilde{\mathbf{v}}_1^{(0)} - \mathbf{e}_x\beta\nabla^2\tilde{\varphi}_1^{(0)} = 0$; $\nabla \cdot \tilde{\mathbf{v}}_1^{(0)} = 0$, the solution to which reads

$$\tilde{\mathbf{v}}_1^{(0)} = \nabla \times (\tilde{S}_1^{(0)} \mathbf{e}_z); \quad \tilde{S}_1^{(0)} = \left\{ \beta(1+y)e^{-y} - \frac{1}{8}\beta^3 y^2 e^{-y} \right\} \cos(x). \quad (44)$$

From solution (44), we note the presence of the β^3 term, which stems from chemio-osmotic flows in the bulk. Therefore, the bulk velocity at this order is not merely proportional to β , as witnessed in the previous order and is actually associated with concentration polarization and induced potential. Note that in the weak-field limit ($\beta \ll 1$), the said chemio-osmotic effect vanishes, since it is nonlinear in β . Nevertheless, one can still capture this effect in weak field limit by carrying out perturbations till $O(\beta^3)$. Finally, we note that there are no contributions to the net free-stream velocity from the velocity field at $O(\delta, \bar{\zeta}_0)$.

2. The $O(\delta, \bar{\zeta}_0)$ solutions

The procedure to derive the $O(\delta, \bar{\zeta}_0)$ solutions are the same as delineated in Sec. IV F. Thus we would only briefly outline the solutions and touch upon the methodology. Once again, we would start with the salt flux balance condition in (26) for $O(\delta, \bar{\zeta}_0^2)$, which furnishes the condition for outer layer salt concentration and reads $[\partial\tilde{c}_1^{(2)}/\partial y]_{y=0} = 0$. However, the concentration at this order satisfies the

equation $\nabla^2 \check{c}_1^{(2)} = \text{Pe} \nabla \cdot (\check{\mathbf{v}}_0^{(0)} \check{c}_1^{(1)})$ and has the following solution:

$$\check{c}_1^{(2)} = -\text{Pe} \beta^2 \left\{ \frac{1}{4} (2y+1) e^{-2y} \left[1 + \frac{1}{2} \cos(2x) \right] + n(1+y) e^{-y} \cos(x) \right\}. \quad (45)$$

The current flux matching at $O(\delta, \bar{\zeta}_0)$ would furnish $\frac{\partial \check{\varphi}_1^{(1)}}{\partial y} \Big|_{y=0} = \frac{1}{2} \beta (2\text{Pe} + 1) (n \sin x + \frac{1}{2} \sin 2x)$. Noting that the potential satisfies the equation $\nabla^2 \check{\varphi}_1^{(1)} = (\beta/2) \partial \check{c}_1^{(2)} / \partial x$, we can deduce the potential at this order, which reads

$$\begin{aligned} \check{\varphi}_1^{(1)} &= \gamma_1(y) \sin(x) + \gamma_2(y) \sin(2x), \\ \gamma_1 &= \frac{n\beta}{18} e^{-y} \{ \text{Pe} \beta^2 (3ye^{-y} + 7e^{-y} - 11) + 18\text{Pe} + 9 \}, \\ \gamma_2 &= -\frac{\beta}{128} e^{-2y} \{ \text{Pe} \beta^2 (4y^2 + 6y + 3) - 32\text{Pe} - 16 \}. \end{aligned} \quad (46)$$

Note that the concentration polarization at $O(\delta, \bar{\zeta}_0^2)$ occurs due to advective transport in the outer layer. This polarization in turn induces its own outer layer potential, while the disturbances in the ion distribution created by the externally applied electric field inside the EDL also contribute to this potential. The physical significance of this potential has already been discussed in the previous subsection. The corresponding inner layer solutions can now be easily deduced, following the same procedure as mentioned in the previous section. We would only mention the solutions here, which read

$$\begin{aligned} \check{\Phi}_1^{(1)} &= \sum_{i=1}^2 \phi_i(Y) \sin(iX); \quad \check{C}_1^{(2)} = -\text{Pe} \beta^2 \left(\frac{1}{4} + n \cos X + \frac{1}{8} \cos 2X \right), \\ \check{\Pi}_1^{(1)} &= -2\check{\Phi}_1^{(1)} + 2 \sum_{i=1}^2 [\gamma_i]_w \sin(iX) + 2\beta \check{\Phi}_o^{(0)} \sin X, \end{aligned} \quad (47)$$

$$\phi_1 = \frac{1}{2} n \beta e^{-Y} (1+Y) + [\gamma_1]_w; \quad \phi_2 = \frac{1}{4} \beta e^{-Y} (1+Y) + [\gamma_2]_w; \quad [\gamma_i]_w = \gamma_i(y=0), \quad i = 1, 2.$$

The solutions for the potential can now be plugged into the momentum equations to deduce the pressure and the X velocity. The X velocity can be subsequently plugged into the continuity equation to estimate the Y velocity. The solutions for the velocities are as follows:

$$\begin{aligned} \check{U}_1^{(1)} &= -\frac{\beta^2}{4} (2n \sin X + \sin 2X) (2 + Ye^{-Y} - 2e^{-Y}) \\ \check{V}_1^{(1)} &= \frac{\beta^2}{2} (n \cos X + \cos 2X) [2Y - 3 + e^{-Y}(Y + 3)]. \end{aligned} \quad (48)$$

Note that the inner layer velocities remain independent of Pe at this order, although the potential and the concentrations strongly depend on the same. The outer velocities satisfy the equation $-\nabla \check{p}_1^{(1)} + \nabla^2 \check{\mathbf{v}}_1^{(1)} - \mathbf{e}_x \beta \nabla^2 \check{\varphi}_1^{(1)} = 0$; $\nabla \cdot \check{\mathbf{v}}_1^{(1)} = 0$. This can be solved subject to appropriate boundary conditions [which can be determined by matching outer and inner layer velocities at the edge of the EDL, at $O(\delta, \bar{\zeta}_0)$; not mentioned here for brevity]. The solutions to the outer layer velocities can be deduced to be of the form

$$\begin{aligned} \check{\mathbf{v}}_1^{(1)} &= \nabla \times (\check{S}_1^{(1)} \mathbf{e}_z); \quad \check{S}_1^{(1)} = \sum_{i=1}^2 f_i(y) \sin(ix), \\ f_1 &= \left\{ -\frac{19}{54} n \beta^4 \text{Pe} + n \beta^2 \left(\frac{13}{54} \text{Pe} \beta^2 - 1 \right) y \right\} e^{-y} + \frac{n \beta^4 \text{Pe}}{9} e^{-2y} \left(y + \frac{19}{6} \right), \\ f_2 &= -\frac{1}{2} \beta^2 y e^{-y} + \text{Pe} \beta^4 e^{-2y} \left(\frac{y^3}{192} + \frac{y^2}{128} \right). \end{aligned} \quad (49)$$

The most interesting point to note from the solutions for velocities is that the outer layer velocities depend on the ionic advection strength (i.e., Pe), although the inner layer velocities are completely independent of them. We further note that there is no contribution to the free-stream velocity at this order as well. However, the next corrections to the velocities do contribute to the far field transport, as we show in the next subsection.

3. Free-stream velocity contribution at $O(\delta, \bar{\zeta}_0^2)$

Here we would only determine the component of the velocity, which contributes to the net flow at far field location, i.e., the component of X velocity independent of X (or, x). To this end, we would require determining the component of inner layer potential at $O(\delta, \bar{\zeta}_0^2)$, which is independent of X . Fortunately, we have already determined the solution to the concentration in the inner layer at this order. This concentration can be used in the charge conservation equation to determine the charge density, which can be subsequently plugged into the Poisson's equation to deduce the potential. Our purpose is only to determine that part of the charge density and potential, which is independent of X . The said component reads (for potential)

$$\tilde{\Phi}_1^* = \bar{\zeta}_0^2 \frac{3Pe\beta^2 n}{16} (1 + Y)e^{-Y} + \text{Periodic terms in } X. \quad (50)$$

The corresponding X velocity is given by

$$\begin{aligned} \tilde{U}_1^{(2)} = & -\frac{n\beta}{144} \{(36 + 72Pe - 43Pe\beta^2 - 27Pe\beta^2 Y)e^{-Y} + 43Pe\beta^2 - 72Pe - 54 + 18e^{-2Y}\} \\ & + \text{periodic terms in } X. \end{aligned} \quad (51)$$

Combining the matching condition for velocity and the outer layer momentum equation, it can be easily determined that the “free-stream” velocity at this order is given by

$$\tilde{u}_{\infty,1}^{(2)} = \frac{\beta n}{144} (54 + 72Pe - 43Pe\beta^2). \quad (52)$$

The most interesting point to note from (52) is that the first contribution to the free-stream velocity at $O(\delta)$ varies nonmonotonically with the applied field strength β . In fact, for $\beta < \sqrt{\frac{54}{73Pe} + \frac{72}{43}}$ the contribution has a net positive sign, which indicates that the free-stream velocity gets reduced as a result [recall Eq. (32)]. However, for larger values of applied field strength, $\tilde{u}_{\infty,1}^{(2)}$ changes sign and actually increases the far field velocity. Moreover, this transition occurs for applied field strength $\beta \sim O(1)$, since $Pe \sim O(1)$, for field-driven flows. Therefore, we can conclude that the first and hence the dominant effect of finite EDL thickness decreases the net free-stream velocity for low applied field strength, whereas the same is augmented for stronger applied fields. To the best of our knowledge, this is first study to explicitly point out such nonmonotonic effect of finite EDL thickness on fluid velocities, in the context of electroosmotic flows over charge-modulated surfaces. We later verify this result by comparing it with numerical simulations.

Finally, we note that, since in the outer layer $\nabla^2 \tilde{\varphi}_1 \neq 0$ in general, we can infer that the bulk is actually not charge-free. In fact, the Poisson's equation in the outer layer suggests that $\tilde{\rho} = \delta^3 [\frac{\beta}{2} \{ \frac{\partial \tilde{c}_1^{(1)}}{\partial x} + \bar{\zeta}_0 \frac{\partial \tilde{c}_1^{(2)}}{\partial x} + \dots \}] + O(\delta^4)$ and hence the electro-neutrality in the bulk is broken at $O(\delta^3)$. Obviously this bulk charge density is much larger for larger values of surface charge. In fact, a large number of previous studies on electrokinetic instabilities [42,44], and others [63] have also concluded that net charges in the EDL protrude into the bulk to create “space-charge” layers.

4. Comparison with previous studies

The present work is closely related to the previous study of Khair and Squires [39], who explored concentration polarization brought about by electrokinetic flows around a charge-modulated surface.

Therefore, it would be insightful to directly compare our results for concentration and potential with those of Khair and Squires to establish a link between the two studies.

There are notable similarities between the analysis done here and that of Ref. [39], albeit with several subtle differences in the definition of the nondimensional numbers (such as Peclet number, field strength, etc.). Further, those authors did not execute a formal matched asymptotic expansion based analysis as outlined here, and hence some of their formulations were directly coming from physical arguments. Notwithstanding such subtle differences, we would denote their quantities for steady dc field with a superscript “*” (such as Pe^*), when directly comparing with our results. To this end, we note the following relations between their nondimensional parameters and the present study: $\hat{\zeta} = \zeta^* = \bar{\zeta}_0$; $\beta^* = \beta\delta$ and $m = 2\text{Pe}$ with $\text{Pe}_e = \text{Pe}^* = \text{Pe}\bar{\zeta}_0\beta$ [there is a factor of “1/2” missing from the definition of Pe_e in Eq. (55) of Ref. [39]]. Note that the parameter m defined there is actually twice the Peclet number defined herein. Those authors carried out a regular perturbation for $\beta^* \ll 1$ and defined the following asymptotic sequences for bulk concentration and potential: $c_b^* = c_\infty^* + \beta^*c_{\beta^*}^* + \dots$; $\phi^* = \beta^*\phi_{\beta^*}^* + \dots$, while the concentrations in the two studies are related as follows: $c^* = \frac{1}{2}c'$. If we recast the above expansions in terms of the nondimensional parameters of the present analysis, they read $c_b^* = 1 + \delta\beta\hat{c}_{\beta^*}^* + \dots$; $\hat{\phi}^* = \delta\beta\hat{\phi}_{\beta^*}^* + \dots$, where overhead caps have been used to denote the nondimensional variables, nondimensionalized with same quantities as that of Ref. [39] (the same as the present study). By inspecting Eqs. (12) and (13) as well as the analysis in the previous subsection, we can note that the terms $\hat{c}_{\beta^*}^*$ and $\hat{\phi}_{\beta^*}^*$ respectively correspond to the variables $\bar{\zeta}_0\bar{\varphi}_1/\beta$ and $\bar{c}_1/2\beta$ of the present work.

For a dc potential of the form, $\zeta = \cos(x)$ (as mentioned in Ref. [39] in Sec. VI), we have to put $n = 0$ in the present analysis. By inspecting Eqs. (39) and (46), we note that in the limit $\beta \rightarrow 0$, the term $\bar{\zeta}_0\bar{\varphi}_1$ takes the form (with $n = 0$):

$$\frac{\bar{\zeta}_0\bar{\varphi}_1}{\beta} = \frac{\bar{\zeta}_0^2}{8}(1 + 2\text{Pe})e^{-2y} \sin(2x) + \dots \quad (53)$$

This is exactly the same as Eq. (62) in Ref. [39], where the excess bulk potential has been reported (ignoring the x/ϵ part, since this comes from the externally applied potential). However, we note from the asymptotic solutions that several other terms appear at $O(\delta)$, which are nonlinear in β [such as $\bar{\varphi}_1^{(0)}$ in Eq. (39)]. Of course, these terms were not reported in the work of those authors, since they only took into account the first corrections from $O(\beta)$ terms.

In regard to the concentration, we note that while balancing the depth averaged fluxes [refer to Eqs. (44)–(50) in Ref. [39]], the authors ignore the contributions from the advective fluxes from the bulk in Eq. (50) of that work. In other words, the flux component $v'c'$, from the outer layer (where v' is the Y velocity) is neglected in the referred work. This eventually leads to the presence of an extra linear term in m , in Eqs. (58), (66), and (67) of Ref. [39]. However, in the present study we have taken into account the contribution of the advective fluxes, as evident from Eqs. (26) herein. Thus, in essence, our results should be equivalent to enforcing $m = 0$ in the solutions of $\hat{c}_{\beta^*}^*$ in Ref. [39]. As such, the solutions of that paper become [refer to Eqs. (67)–(72) in Ref. [39], with $m = 0$]

$$\hat{c}_{\beta^*}^* = -\bar{\zeta}_0 e^{-y} \sin(x) - \text{Pe}\beta\bar{\zeta}_0^2(2y + 1)e^{-2y} \left[\frac{1}{8} + \frac{1}{16} \cos(2x) \right] + \dots \quad (54)$$

By inspecting Eqs. (38) and (45) of the present work, we note that Eq. (54) matches exactly with $\bar{c}_1/2\beta$ (recall that $n = 0$ here). Therefore, we have demonstrated that our analysis can successfully reproduce at least the first corrections to the concentration and potential profile derived previously in Ref. [39]. Furthermore, our analytical solutions also compare well with independent numerical simulations (presented in the forthcoming section), which also supports the accuracy of the current asymptotic analysis. We have also compared the contours of concentration perturbation of our solutions to those of Ref. [39]. The plots have been included in Appendix B.

G. The $O(\delta^2)$ problem

Ionic advection (Pe) directly influences the quantities in the inner layer at $O(\delta^2)$. Therefore, for completeness, we would also attempt to solve for the $O(\delta^2)$ variables. Since the solution procedure is exactly the same as described in the previous order of δ , we would not describe the same for brevity. The details of the solutions are mentioned in Appendix C. In this section, we would only mention the correction to the free-stream velocity at $O(\delta^2)$. The detailed solutions indicate that the said contribution in fact comes at $O(\delta^2, \bar{\zeta}_0^2)$, just like the solutions at $O(\delta)$, and is given by

$$\tilde{u}_{\infty}^{(2)} = \bar{\zeta}_0^2 \tilde{u}_{\infty,2}^{(2)}; \quad \tilde{u}_{\infty,2}^{(2)} = -\beta n \left(\frac{233}{192} + \frac{11}{8} \text{Pe} \right) - n\beta^3 \left(\frac{5}{16} \text{Pe} \right) + \frac{17}{1152} \text{Pe} \beta^5 n. \quad (55)$$

Detailed calculations show that chemio-osmotic forces due to concentration polarization in the outer layer contribute to the free-stream velocity at $O(\delta^2)$. Note that the component $\tilde{u}_{\infty,2}^{(2)}$ is linearly dependent on the advection strength. However, the dependence on β , i.e., the applied field strength, is nonlinear and nonmonotonic as in the previous order. For relatively smaller values of β , the $\tilde{u}_{\infty,2}^{(2)}$ component leads to an increase in the free-stream velocity. Finally, we note that the total free-stream velocity is given by

$$\tilde{u}_{\infty} = \tilde{u}_{\infty,0}^{(0)} + \bar{\zeta}_0^2 \tilde{u}_{\infty,0}^{(2)} + \delta \bar{\zeta}_0^2 \tilde{u}_{\infty,1}^{(2)} + \delta^2 \bar{\zeta}_0^2 \tilde{u}_{\infty,2}^{(2)} + \dots \quad (56)$$

The expressions for the various components in (56) have been given in Eqs. (32), (37), (52), and (55). Note that, if one ignores the contribution from higher order terms involving $\bar{\zeta}_0$ (for low surface potential), the free-stream velocity is not affected by finite EDL thickness, even if $\beta \sim O(1)$. In fact, it can be concluded that the far field velocity, to the leading order of $\bar{\zeta}_0$, remains unchanged so far as $\beta < O(\bar{\zeta}_0^{-1})$. We further note that, in the weak field limit, i.e., for $\beta \ll 1$, neglecting any nonlinear contribution from β , we find

$$[\tilde{u}_{\infty}]_{\beta \ll 1} = -n\beta + \frac{\beta \bar{\zeta}_0^2}{48} (2n^3 + 3n) + \delta \bar{\zeta}_0^2 \frac{\beta n}{144} (54 + 72\text{Pe}) - \delta^2 \bar{\zeta}_0^2 \beta n \left(\frac{233}{192} + \frac{11}{8} \text{Pe} \right). \quad (57)$$

We recall that the quantity Δu_{∞} , as defined in Sec. III, has the following definition based on analytical solutions:

$$\Delta \tilde{u}_{\infty} = \delta \bar{\zeta}_0^2 \tilde{u}_{\infty,1}^{(2)} + \delta^2 \bar{\zeta}_0^2 \tilde{u}_{\infty,2}^{(2)} + \dots \quad (58)$$

Finally, we recall that the actual nondimensional free-stream velocity is given by

$$u_{\infty} = \bar{\zeta}_0 \tilde{u}_{\infty} \text{ and } \Delta u_{\infty} = \bar{\zeta}_0 \Delta \tilde{u}_{\infty}. \quad (59)$$

We reiterate that the quantity $\Delta \tilde{u}_{\infty}$ embodies the effect of finite EDL thickness on the free-stream velocity, highlighting the difference between a full PNPNS based approach and the ‘‘naive’’ Smoluchowski slip velocity approach.

V. RESULTS AND DISCUSSION

This section primarily focuses on three aspects of the flow dynamics, (1) the potential and concentration distribution in the domain, (2) the free-stream velocity, and (3) the overall flow dynamics, as visualized through streamlines. For this entire section we would stick to $\text{Pe} = 0.5$, following the assertion of Saville [2] with regard to field-driven phenomena. We would emphasize the effect of the following parameters on the foresaid variables: (a) the applied field strength (β), (b) the EDL thickness, and (c) the magnitude of the potential, $\bar{\zeta}_0$.

A. Potential and concentration distribution

We start our discussions with Fig. 2, where variations in the potential [in Fig. 2(a)] and the concentration [in Fig. 2(b)] have been depicted as a function of y , at $x = 2.3833$, for three choices of

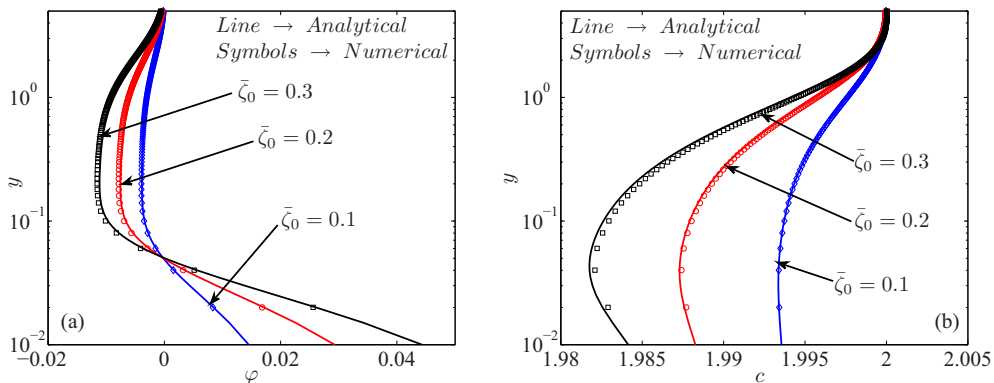


FIG. 2. Comparison between numerical (symbols) and analytical (solid lines) solutions for (a) φ vs y and (b) c vs y for three different values of $\bar{\zeta}_0 = 0.1, 0.2$, and 0.3 . The concentration and potential profiles have been plotted at an axial location of $x = 2.3833$. Values of other relevant parameters are as follows: $Pe = 0.5$, $\beta = 2.1$, $\delta = 0.025$, and $n = 1$.

$\bar{\zeta}_0 = 0.1, 0.2$ and 0.3 in the thin EDL limit ($\delta = 0.025$), while values of all other relevant parameters are mentioned in the caption. We have plotted both analytical (solid lines) and numerical (markers) solutions for comparison, where a combined uniformly valid expansion has been plotted to represent the analytical solutions. First, we note that the two solutions show reasonably good agreement throughout the domain, the agreement being better for lower values of $\bar{\zeta}_0$. Both figures confirm our earlier assertion that (see the analysis in Sec. IV) the application of external field and the associated flow results in concentration polarization in the outer layer [see Fig. 2(b)], which in turn, leads to an excess induced potential in the bulk. The change in the salt concentration and the resulting excess potential in the bulk is naturally larger for larger values of $\bar{\zeta}_0$. We reiterate that the first concentration polarization in the bulk occurs at $O(\delta, \bar{\zeta}_0)$, which basically results in a “salt-depleted” zone just outside the EDL [see Fig. 2(b)] as indicated by concentrations lower than 2 (neutral, far field concentration) in that region. A number of previous studies, including those of Dukhin and Shilov [67,68], and more recently those of Chu and Bazant [69] and Khair and Squires [39] have explored similar concentration polarization phenomena around the EDL in great detail. Therefore, a highly insightful account of this phenomenon can be found in the foresaid studies. Nevertheless, for the sake of completeness, here we briefly discuss about the concentration polarization in the bulk. The primary source of such variation in the concentration stems from nonuniform current and salt fluxes in the EDL, which is primarily driven by the externally applied electric field [39]. These fluxes can be viewed as a result of the broken symmetry due to the application of the external electric field. Since the concentration distribution inside the EDL is not uniform (but the external field is, at least to the leading order), the resulting fluxes are also not uniform in nature. Therefore, these fluxes are not divergence free. As a result, the EDL essentially “spills out” ions into the bulk in certain places and extracts ions from others. This phenomenon of “spilling out” and extraction is effectively manifested through the Eqs. (26). The final result of such nonuniform flow of ions between the EDL and the bulk is the polarization of concentration in the bulk. The fact that the said polarization is driven by the external field can be easily inferred from Eqs. (38) and (40), where we note that the corrections to the concentration (i.e., the polarization terms) are proportional to β , i.e., the external field strength. The periodic nature of these correction terms also support the assertion that ions are indeed spilled out in some places and extracted at others, from the bulk.

We next focus on Fig. 3, where variations in the potential [in Fig. 3(a)] and the concentration [in Fig. 3(b)] have been depicted as a function of y , at $x = 2.3833$, for four choices of $\beta = 0.1$ (weak field limit), 1.7, 3.3, and 4.5 in the thin EDL limit (with $\delta = 0.025$), while values of all other relevant parameters are mentioned in the caption. We have plotted both analytical (solid lines, uniformly valid combined expansion) and numerical (markers) solutions for comparison. Reasonably good

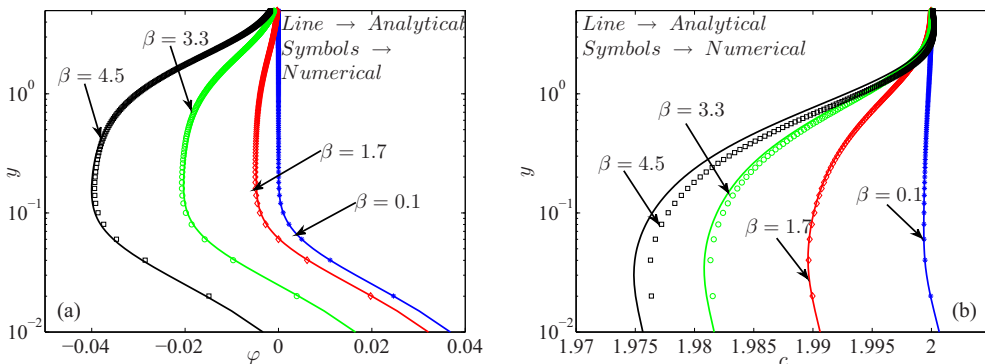


FIG. 3. Comparison between numerical (symbols) and analytical (solid lines) solutions for (a) φ vs y and (b) c vs y for four different values of $\beta = 0.1, 1.7, 3.3,$ and 4.5 . The concentration and potential profiles have been plotted at an axial location of $x = 2.3833$. Values of other relevant parameters are as follows: $Pe = 0.5$, $\bar{\zeta}_0 = 0.2$, $\delta = 0.025$, and $n = 1$.

agreement can be noted between the two solutions, the agreement being better for lower values of β . The overall trend of the variation remains the same as shown in the previous figure(s) (see Fig. 2). As expected, the extent of concentration polarization and the associated induced excess potential in the bulk intensify as the applied field strength is augmented. We recall that in the leading order of δ , i.e., when the Helmholtz-Smoluchowski formulation is applied, there is no concentration polarization in the bulk. Hence the variations shown in the previous two figures (Figs. 2 and 3) stem from finite EDL thickness combined with the effects of applied external field and heterogeneous fluid motion. In Fig. 3(b) it is interesting to note the relatively larger discrepancies between the analytical and numerical solutions of c , as compared to those for the potential. However, we would like to point out that in the context of overall variations, the discrepancies are still small. In general it is hard to pinpoint to one exact reason for such relative differences. This is because the accuracy of perturbation solutions strongly depends on the convergence of the asymptotic series [58]. However, as a rule of thumb it can be noted that singular perturbation generally produces divergent series and hence is valid only in the limit $\delta \rightarrow 0$ [58]. More importantly, we should note that while evaluating \bar{c}_2 , we have only deduced the leading corrections of $O(\bar{\zeta}_0^2)$ at this order of δ (refer to Appendix C). On the other hand, for potential, the first two corrections in terms of $\bar{\zeta}_0$ at $O(\delta^2)$ were determined. Since the discrepancies between the numerical and analytical solutions for c are very small, it seems entirely plausible that this lack of enough correction terms might cause the apparent mismatch.

Figure 4 showcases the variations in the same quantities [potential in Fig. 4(a) and concentration in Fig. 4(b)], at the same location, as functions of y , for four different values of $\beta = 0.5, 1, 3,$ and 5 , while values of all other parameters are mentioned in the caption. Here we have only plotted the results from the numerical simulations, as attributable to the larger choice of $\bar{\zeta}_0 (= 3)$. We can very easily infer that the quantities in Figs. 4(a) and 4(b) demonstrate augmented versions of the same variations as noted in Figs. 3(a) and 3(b). Because of larger strength of surface charge (or, equivalently, $\bar{\zeta}_0$) and relatively thicker EDL ($\delta = 0.1$), the concentration in the bulk shows larger polarization. The resulting excess potential in the bulk also has a larger magnitude, as compared to the previous figures. It is interesting to note that the polarity of the salt concentration in the bulk reverses, as β is increased. We observe that for lower values of β a “salt-depletion” zone exists just outside the EDL [refer to Fig. 3(b)], while for larger β , excess amount of salt is present in the bulk at the same location.

B. Free-stream velocity

The main quantity of interest in this section would be Δu_∞ , which signifies the change in the free-stream velocity brought about by finite EDL thickness. We first concentrate on the variation in

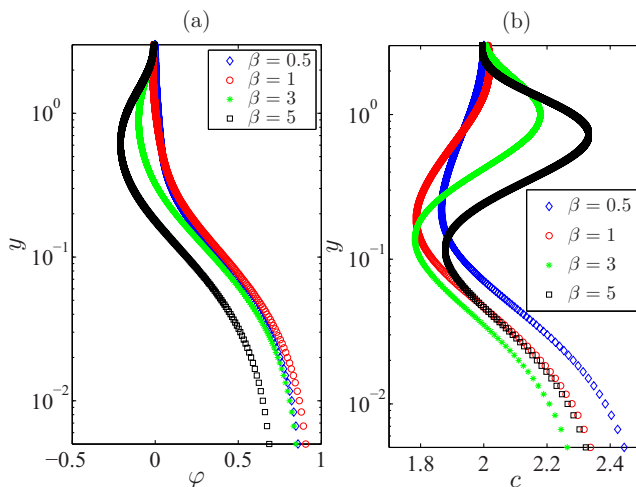


FIG. 4. Plot (numerical only) of (a) potential (φ) vs y and (b) concentration (c) vs y , for four different values of $\beta = 0.5, 1, 3,$ and 5 . Values of other parameters are given by $\delta = 0.1, n = 1, \bar{\zeta}_0 = 3,$ and $Pe = 0.5$.

Δu_∞ as a function of β in the thin EDL limit ($\delta = 0.025$) for three different values of $\bar{\zeta}_0 = 0.1, 0.2,$ and 0.3 in Fig. 5, while values of all other relevant parameters are mentioned in the caption. In the inset, the normalized free-stream velocity, i.e., $u_\infty/u_{\infty,\delta=0}$ has been plotted as a function of β (for same choices of parameters), for a complete representation. We have plotted numerical (markers) as well as analytical (solid lines) solutions for comparison. First, we note that reasonably good agreement between the two can be observed, especially considering the fact that Δu_∞ captures the effects of only the perturbation terms from an analytical point of view. Since we are comparing the numerical solutions to the analytical ones, we have subtracted $\bar{\zeta}_0 \bar{u}_{\infty,0}^{(0)}$ from both the solutions

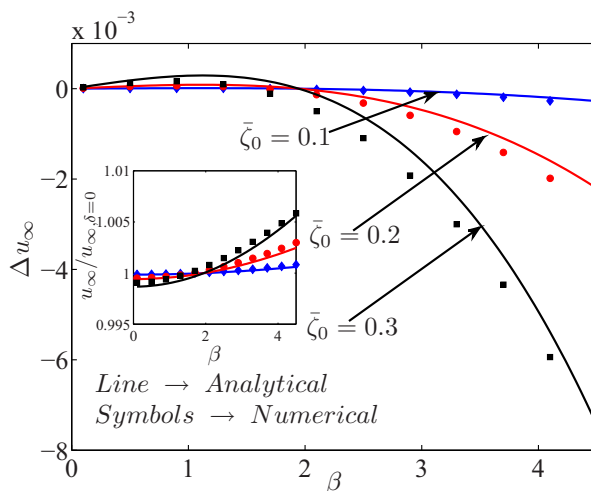


FIG. 5. Comparison between analytical and numerical solutions of $\Delta u_\infty = u_\infty - u_{\infty,\delta=0}$ vs β for three different values of $\bar{\zeta}_0 = 0.1, 0.2,$ and 0.3 . In the inset we have demonstrated the normalized total free-stream velocity, i.e., $u_\infty/u_{\infty,\delta=0}$ vs β for the same values of $\bar{\zeta}_0$. The symbols represent the numerical solutions, whereas the lines show the analytical solutions. Values of other relevant parameters are $\delta = 0.025, n = 1,$ and $Pe = 0.5$.

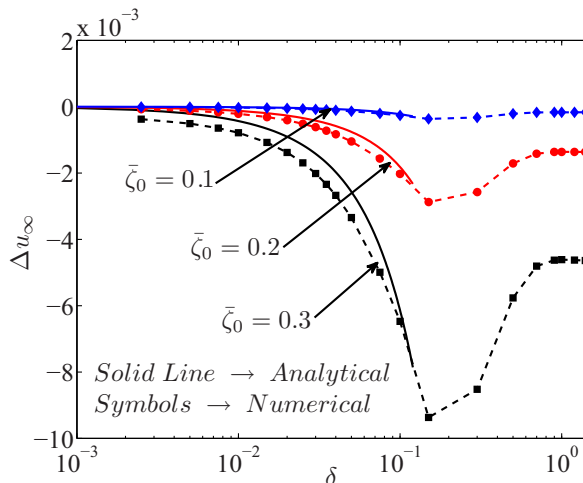


FIG. 6. Comparison between numerical (markers) and asymptotic (solid lines) solutions for Δu_∞ vs δ , for three different values of $\bar{\zeta}_0 = 0.1, 0.2, 0.3$. Values of other relevant parameters are given by $n = 1$, $Pe = 0.5$, and $\beta = 2.8$.

to evaluate the quantity Δu_∞ . The second most interesting point to note is that the assertion made in Sec. IV E, that the net change in the free-stream velocity (i.e., Δu_∞) varies nonmonotonically with β , is verified here, since the numerical solutions also show similar variations. We note that the free-stream velocity magnitude decreases first, for low values of β . After the field strength crosses a threshold value, the magnitude of the free-stream velocity keeps on increasing with the applied field strength. While it is relatively difficult to visualize these nonmonotonic variations in the numerical solutions from the main figure, the said variation becomes apparent in the inset. Note that a nonmonotonic variation in Δu_∞ would indicate that the quantity $u_\infty/u_{\infty,\delta=0}$ should vary from a value less than 1 to values larger than 1. This is exactly what we observe from the inset of Fig. 5, where both numerical and analytical solutions exhibit the said variation, thus validating the assertion made based on the analytical solutions. We further note that the numerical and analytical solutions also show reasonably good agreement in the inset of Fig. 5. The said nonmonotonic variation of course stems from the changes incurred by the application of the external field on the ionic species concentrations as well as the potential in both inner and outer layers. However, the magnitude of the changes to the free-stream velocity as demonstrated in Fig. 5 is quite small, roughly $O(10^{-3})$. This is because the analytical solutions remain valid in thin EDL limit ($\delta \ll 1$) for low surface potential strength ($\bar{\zeta}_0 \ll 1$), while the changes in the free-stream velocity first occurs at $O(\delta \bar{\zeta}_0^2)$. Nevertheless, the analytical solutions correctly explains the physics of the problem, wherein lies the significance of the same. Later, when we focus solely on numerical solutions for larger potentials and thicker EDLs, more significant variations in the free-stream velocity can will be witnessed.

We next move to Fig. 6, where the variations Δu_∞ in as a function of EDL thickness δ has been depicted, for three different values of $\bar{\zeta}_0 = 0.1, 0.2$, and 0.3 , while values of all other relevant parameters are mentioned in the caption. Here, we have plotted the numerical solutions (markers) for a wide range of EDL thickness, while the analytical solutions (lines) have been plotted only for thin EDL limit. Again, reasonably good agreement is observed between the analytical and numerical solutions, the agreement being better for lower values of potential strength. Note that for the choice of β in this figure, the free-stream velocity actually increases in magnitude as denoted by the negative values of the quantity Δu_∞ . However, the most interesting point to note from Fig. 6 is that Δu_∞ varies nonmonotonically with δ as well, for all three values of $\bar{\zeta}_0$. In fact, for $\delta \sim 0.15$, Δu_∞ goes through a maximum (magnitude-wise) and the effect of EDL thickness on

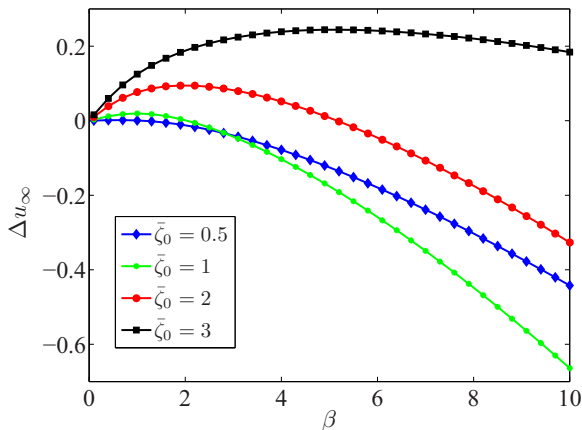


FIG. 7. Plot (numerical only) of Δu_∞ vs β for four different values of $\bar{\zeta}_0 = 0.5, 1, 2,$ and 3 , while values of other parameters have been chosen as $n = 2, \text{Pe} = 0.5, \delta = 0.1$.

free-stream velocity diminishes for larger values of δ . This indicates that the overall flow dynamics is most effected by a particular EDL thickness (i.e., for a particular salt concentration), while for larger EDL thickness the influence slowly fades away, owing to dilution of the solution (note that larger EDL thickness denotes more dilute solutions). Although such intriguing behavior cannot be properly explained by the analytical solutions, it can nonetheless offer us some clues in this regard. Note from the analysis of Secs. IV F and IV G that the $O(\delta)$ and $O(\delta^2)$ contributions to the free-stream velocity tend to oppose each other, at least for low to moderate values of $\beta [\sim O(1)]$. As we increase the EDL thickness, the effect of the higher order terms in δ become more prominent and after the EDL thickness goes beyond a certain value, the higher order terms actually begin to dominate as evidenced in Fig. 6. Of course, at this juncture the whole premise of the asymptotic analysis breaks down and quantitative matching cannot be expected. However, from a qualitative point of view, these solutions go some way towards explaining the nonmonotonic behavior under consideration.

Figure 7 depicts the variations in Δu_∞ (numerical only) as a function of the applied field strength (β), for different choices of $\bar{\zeta}_0 = 0.5, 1, 3,$ and 5 , while values of all other relevant parameters are mentioned in the caption. This figure is basically an augmented version of Fig. 5, where the same variation was showcased for thinner EDL and lower surface potential. The same overall qualitative features thus hold for the present figure as well. For example, we note that the free-stream velocity (magnitude) first decreases for smaller values of applied field strength and upon further increasing β the trend is reversed; the exact same variation in Δu_∞ was noted in Fig. 5. However, one unique feature to be noted in the present figure is that the threshold value of β , beyond which the free-stream velocity starts increasing (i.e., the trend is reversed), seems to depend on magnitude of $\bar{\zeta}_0$. In fact, as the overall strength of the EDL potential is augmented, this threshold field strength increases, as evident from the figure. This is nicely reflected in the variation for $\bar{\zeta}_0 = 3$, wherein the threshold lies beyond the range of β chosen for the present figure.

We end the discussion in this section with Fig. 8, where Δu_∞ has been plotted (numerical solutions only) as a function of $\bar{\zeta}_0$, for three different values of applied field strength ($\beta = 1, 2,$ and 5), while the values of all other relevant parameters are mentioned in the caption. This figure is consistent with the previous figures, since we note that for a fixed value of $\bar{\zeta}_0$, Δu_∞ changes sign from positive to negative, as the value of β is increased. The reason for such behavior has already been discussed in detail in relation to the earlier figures. However, one very interesting point to note is that the change in the free-stream velocity (i.e., Δu_∞) goes through an extremum (magnitude-wise) when the value of $\bar{\zeta}_0$ is increased. This extremum is particularly clear for $\beta = 5$ and is slightly visible for $\beta = 2$.

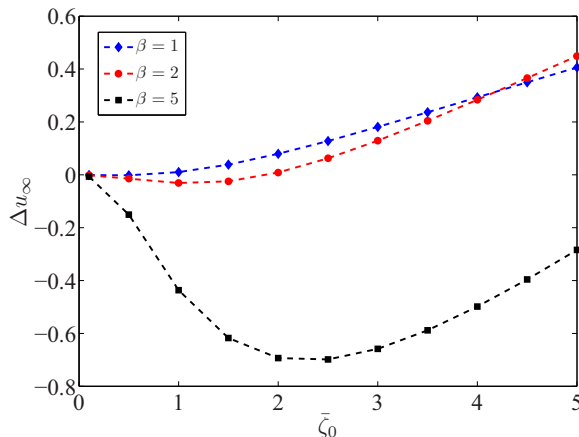


FIG. 8. Plot (numerical only) of Δu_∞ vs $\bar{\zeta}_0$, for three different values of $\beta = 1, 2,$ and 5 , while values of other relevant parameters have been chosen as $n = 1, \delta = 0.1$ and $Pe = 0.5$.

After this point, the magnitude of Δu_∞ decreases for $\beta = 5$, while the same increases for lower values of β . In particular, for $\beta = 1$ and 2 , the quantity Δu_∞ is positive, which indicates a decrease in the magnitude of the free-stream velocity. For $\beta = 5$, the free-stream velocity always increases for the range of $\bar{\zeta}_0$ chosen here. The reason for such behavior can be traced back to the previous figure (Fig. 7), where we have already demonstrated that the threshold value of β , for which the sign change in the quantity Δu_∞ occurs (i.e., the contribution from finite EDL thickness reverses), keeps on increasing as $\bar{\zeta}_0$ gets larger.

C. Streamline patterns

In this section, we would only focus on the numerical solutions to study the overall flow structure, as indicated by the streamline patterns. To this end we first focus on Figs. 9(a)–9(d), where the streamline patterns have been shown for four separate values of $\beta = 1, 5, 10,$ and 20 , while values of all other relevant parameters are mentioned in the caption. We note sharp changes in the overall flow patterns as the external field strength is increased. For low values of β (1 and 5), there are two recirculation rolls located near the wall, which are the usual features for flows with patterned surface charges [70]. However, as the strength of the externally applied field is augmented (to $10, 20$), the rolls tend to disappear and the streamlines straighten all over the flow domain. This intriguing effect can in fact be related to Figs. 5 and 7, where we have depicted that the free-stream velocity increases as the value of β goes beyond a certain threshold. This would naturally indicate increased net throughput and smaller rolls, which is aptly reflected in Figs. 9(a)–9(d).

We next move on to our final figure, i.e., Figs. 10(a)–10(d), where the streamline patterns have been shown for four different values of $\bar{\zeta}_0 = 0.2, 1, 5,$ and 10 , while values of all other relevant parameters are mentioned in the caption. We note that the overall streamline patterns are less sensitive to the changes in potential magnitude as compared to the changes in the applied field strength. Further note that, for the particular value of β chosen, increasing the potential leads to increase in recirculation flow in the domain. This is clear from the fact that for $\bar{\zeta}_0 = 0.2$, only one recirculation roll is present centrally in the domain. However, as $\bar{\zeta}_0$ is gradually increased, the streamlines around this recirculation roll get more and more distorted and finally give away to a second recirculation roll, which becomes prominent for $\bar{\zeta}_0 = 10$. Therefore, one can conclude that increases in the surface potential and applied field strength tend to influence the overall flow patterns in opposite fashion. While, increased applied field strength tends to phase out recirculation rolls and straightens the streamlines, an increased potential magnitude makes the streamlines more distorted

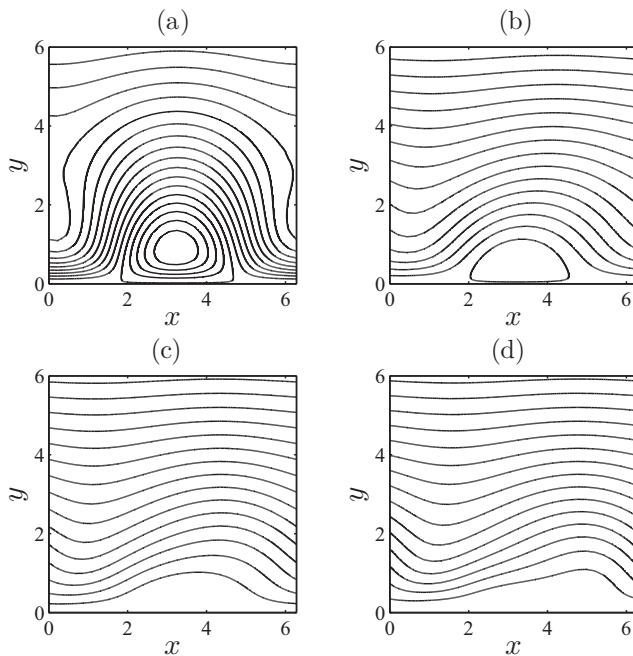


FIG. 9. Evolution of streamline contours (numerical only) for increasing β as (a) 1, (b) 5, (c) 10, and (d) 20. Values of other parameters have been chosen as $n = 0.1$, $\delta, \bar{\zeta}_0 = 2$, and $Pe = 0.5$.

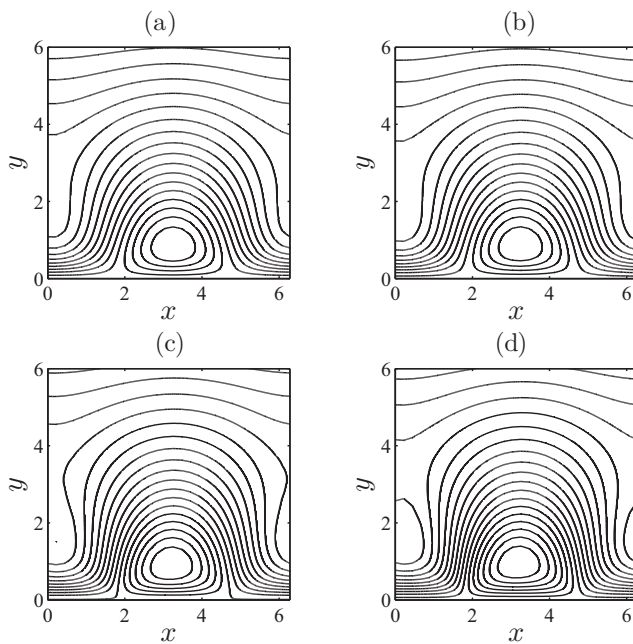


FIG. 10. Evolution of streamline contours (numerical only) with gradual increase in $\bar{\zeta}_0$ as (a) 0.2, (b) 1, (c) 5, and (d) 10. Values of other relevant parameters are given by $n = 0.1$, $Pe = 0.5$, $\beta = 1$, and $\delta = 0.1$.

and eventually leads to the formation of a second recirculation roll. We recall that although the analytical solutions of Sec. IV is only valid in the limit $\bar{\zeta}_0 \ll 1$, we can still have some qualitative idea regarding the evolution of the streamlines from the perturbation solutions. We note from the asymptotic solutions that the higher order terms of $\bar{\zeta}_0$ contribute more periodic (or, sinusoidal terms) terms to the overall stream functions, which naturally leads to increased recirculation in the flow. This is ultimately manifested through the appearance of new recirculation rolls for larger values of $\bar{\zeta}_0$, as noted in Fig. 10(d).

VI. CONCLUSIONS

We have solved the fully coupled Poisson-Nernst-Planck-Navier-Stokes model in the presence of patterned surface charge, to bring out the effects of finite EDL thickness on the fluid and charge dynamics in an electro-osmotically actuated flow. To this end, we have performed numerical simulations for a wide range of applied field strengths, surface potentials and EDL thicknesses, while assuming the ionic Peclet number to remain $\sim O(1)$. We have further derived asymptotic solutions valid for thin EDL thickness and low surface potentials. We have used singular perturbation to resolve the dynamics within the EDL, while a subsequent regular asymptotic analysis has been applied to deduce the effect of small characteristic surface potential. While deriving the asymptotic solutions, we have assumed both Pe and β to remain $\sim O(1)$. While representing the results, we have used net change in the free-stream velocity owing to finite EDL thickness as one of the main indicators of the overall flow. We show that reasonably good agreement between the asymptotic and numerical solutions can be observed within an appropriate regime of validity of the former.

Our results reveal that the applied field strength influences the free-stream velocity nonmonotonically, when finite EDL thickness is taken into account. For lower electric field strength, the free-stream velocity tends to decrease, while beyond a critical field strength the far field velocity increases with β . Both asymptotic and numerical solutions reach this same conclusion. The numerical simulations predict that the said threshold value of the applied electric field strength increases with increasing $\bar{\zeta}_0$. Our study further shows that the effect of finite EDL thickness on the free-stream velocity is most prominent for a particular EDL thickness (around $\delta \sim 0.15$). We have also demonstrated that increments in the potential strength (i.e., $\bar{\zeta}_0$) and the applied field strength (β) tend to influence the flow patterns in the opposite ways. While increases in the field strength tends to remove recirculation rolls from the flow domain, increases in $\bar{\zeta}_0$ leads to generation of additional rolls and more distortions in the shape of the streamlines. These results can be potentially consequential in designing micro-scale devices of modern scientific and technological relevance, which employ electrokinetic flow actuation and mixing processes.

APPENDIX A: DETAILS OF NUMERICAL SIMULATIONS

A. Domain and grid distribution

Since we are considering a semi-infinite region in the present study, the height of the domain (H) should be such that all the velocity gradients vanish as well as the potential reaches zero (i.e., the ‘‘far field’’ conditions in (7) are satisfied), when $y = H$. The best way to meet this criterion is to choose the domain height based on the EDL thickness. Accordingly, for $\delta < 1$, we have taken $H = 10$, while for larger values of δ , the domain height was taken to be $H = 20$. The whole domain was divided into rectangular grids of nonuniform density. The length along the x axis was divided into 100 uniformly spaced grid points, while along the y axis the grid points were nonuniformly placed. In an effort to capture the variation within the EDL properly, a larger number of grid points were taken near the wall. To this end, the grid sizes were increased continuously from the wall, with a specified ratio between the first and the last grid. COMSOL Multiphysics 4.4 allows us to take the said ratio in geometric sequence, where the grid sizes are increased exponentially. In our simulations, we have taken 1000 grid points along y axis, while the grid sizes were increased geometrically, the element ratio being 0.0001. As an example of variations in the grid size (and their relative sizes to the

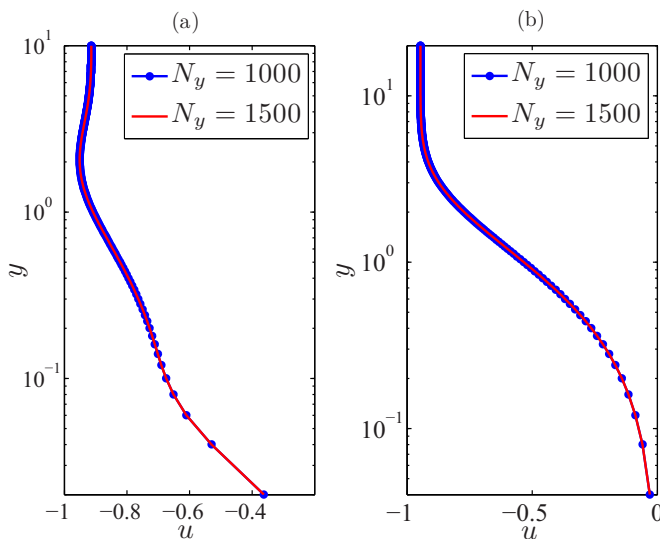


FIG. 11. Grid independence test of the numerical simulations for u vs y data at $x = 1.95$, for (a) $\delta = 0.025$ and (b) $\delta = 1.2$, while other parameters have been chosen as $\bar{\zeta}_0 = 1$, $\beta = 1$, $n = 1$, $Pe = 0.5$. The simulations have been carried out for two different grid distributions along y directions, $N_y = 1000$ and 1500 , while the number of grids in the x direction has been taken as 100 . The successive element ratio has been chosen as 0.0001 .

domain), we note that for $\delta = 0.025$, the minimum grid size was 0.062×10^{-5} near the wall, inside the EDL. In the same simulation, the largest grid size near the top of the domain was 0.062×0.092 .

B. Grid independence

To ensure grid independence of the solutions, we have tested the results from our numerical simulations for the following values of EDL thickness, (a) $\delta = 0.025$ (thin EDL) and (b) $\delta = 1.2$ (thick EDL). For case (a), the numerical simulations were carried out for $H = 10$ with $N_y = 1000$ and 1500 grid points along the y direction (number of grid points along the x direction has been kept the same). For case (b), the same number of grids were chosen, with $H = 20$. In both the cases, the same successive ratio of the neighboring elements has been maintained. Figures 11(a) and 11(b) depict the results of grid independence test for the variation in the X velocity (u) with the y coordinate, at a location $x = 1.95$. The plots clearly indicate that grid independence is indeed achieved at 1000 grid points along the y direction.

C. Domain size independence

To ensure that the results for the free-stream velocity are independent of the domain height (H) along the y direction, we have carried out two sets of numerical simulations for the same EDL thicknesses as mentioned in part (a). For $\delta = 0.025$, simulations were executed for $H = 10$ and 20 , with 1000 and 2000 grid points along the y axis respectively. On the other hand, for $\delta = 1.2$, simulations were executed for $H = 20$ and 30 , with 1000 and 1500 grid points, respectively. Figures 12(a) and 12(b) compare the corresponding results for the X velocity (u) as a function of y (same x location), for different domain sizes. Both the figures indicate that the velocity distributions are indeed independent of H , for its lower values, i.e., for $H = 10$ in (a) and $H = 20$ in (b). Figures 11 and 12 thus ensure that the results from our numerical simulations are independent of the choice of the domain height and grid size.

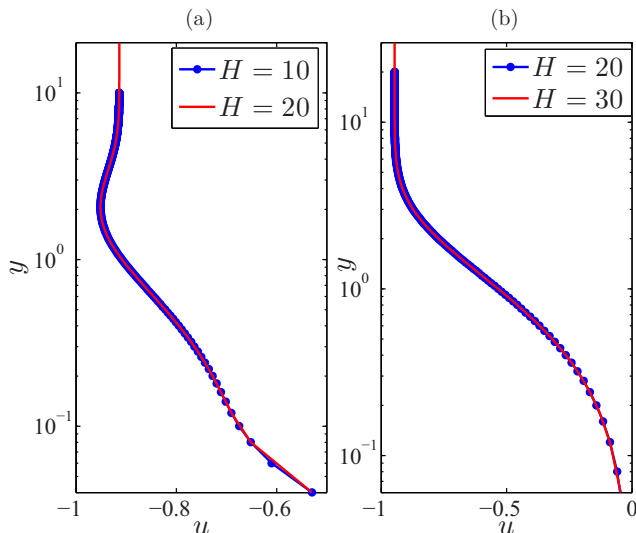


FIG. 12. Domain independence test of the numerical simulations for u vs y data at location $x = 1.95$, for (a) $\delta = 0.025$ and (b) $\delta = 1.2$, while other parameters have been chosen as $\bar{\zeta}_0 = 1$, $\beta = 1$, $n = 1$, $Pe = 0.5$. The simulations have been carried out for two different domain sizes along the y directions: (a) $H = 10$ ($N_y = 1000$) and 20 ($N_y = 2000$), and (b) $H = 20$ ($N_y = 1000$) and 30 ($N_y = 1500$). The successive element ration has been chosen as 0.0001 .

APPENDIX B: CONTOUR PLOT OF CONCENTRATION POLARIZATION

For completeness, we will compare the contours of our concentration profile, from the analytical solutions in Sec. IV with those reported by Khair and Squires [39] in Fig. 8 of their work. Since our study is valid for low to $O(1)$ values of Pe , we would only compare our contour plots to those in the first row of the said figure. Figure 13 demonstrates the contours of \bar{c}_1/β for two different values of Pe , chosen based on the value of Pe_e reported in Fig. 8 of Ref. [39]. The color scheme has been chosen to be the same as in Ref. [39], while the values of all other relevant parameters are mentioned in the caption. The contours of concentration perturbation as shown here are remarkably similar to those of Ref. [39], thus establishing a strong link between the two studies.

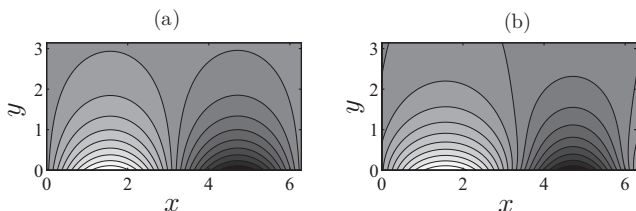


FIG. 13. Contour plot of concentration perturbation for comparison with Fig. 8 of Ref. [39]. We have plotted the quantity \bar{c}_1/β for (a) $Pe = 0.05$ ($Pe_e = 0.01$) and (b) $Pe = 5$ ($Pe_e = 1$), while other parameters have been chosen as, $\bar{\zeta}_0 = 0.2$, $\delta = 0.025$, $\beta = 1$. The white regions indicate a concentration-depleted region, while the dark regions are salt-rich zones. These contours are very similar to those of Ref. [39].

**APPENDIX C: EXPRESSIONS FOR CONCENTRATION, POTENTIAL,
AND VELOCITIES AT $O(\delta^2)$**

A. Concentration profile

The first correction to the concentration in the outer layer at $O(\delta^2)$ comes at $O(\delta^2, \bar{\zeta}_0^2)$ and reads

$$\bar{c}_2 = \bar{\zeta}_0^2 \bar{c}_2^{(2)} + \dots; \quad \bar{c}_2^{(2)} = h_0(y) + h_1(y) \cos(x) + h_2(x) \cos(2x); \quad (C1)$$

here

$$\begin{aligned} h_0(y) &= -\frac{\text{Pe}\beta^2}{32} e^{-2y} \left\{ 2\beta^2 \left(y^2 + y + \frac{1}{2} \right) - 16y - 24 \right\}; \quad h_1(y) = D_1 e^{-y}, \\ h_2(y) &= K_1 e^{-2y} + \frac{1}{4} \text{Pe}\beta^2 y e^{-2y} \left(1 - \frac{1}{8} \beta^2 y - \frac{1}{16} \beta^2 \right); \quad D_1 = -n\beta^2(2\text{Pe} + 1), \\ K_1 &= -\frac{1}{2} \left[D_2 - \frac{1}{4} \text{Pe}\beta^2 \left(1 - \frac{\beta^2}{16} \right) \right]; \quad D_2 = -\beta^2(\text{Pe} + 1). \end{aligned} \quad (C2)$$

The inner layer concentration till $O(\delta^2, \bar{\zeta}_0)$ is given by

$$\bar{C}_2 = \bar{\zeta}_0 \bar{C}_2^{(1)} + \dots; \quad \bar{C}_2^{(1)} = 2\beta \sin X(Y + e^{-Y}). \quad (C3)$$

B. Solution for potential

The inner layer potential is given by [till $O(\delta^2, \bar{\zeta}_0)$]

$$\bar{\Phi}_2^{(0)} = -\frac{1}{2}(1+Y)e^{-Y} \cos X; \quad \bar{\Phi}_2^{(1)} = \sum_{i=1}^2 j_i(Y) \sin(iX) - \sum_{i=1}^3 \frac{A_i}{i} \cos(iX). \quad (C4)$$

The constants A_i 's are given by $A_1 = \frac{3}{32} \text{Pe} \beta^2 (4n^2 + 1)$; $A_2 = \frac{3}{4} \text{Pe} \beta^2 n$; $A_3 = \frac{9}{32} \text{Pe} \beta^2$. The functions $j_i(Y)$ have very algebraically complicated expressions. The MAPLE files containing the expressions can be made available upon request to the authors. The potentials in the outer layer are given by

$$\begin{aligned} \bar{\varphi}_2^{(1)} &= \sum_{i=1}^2 J_i(y) \sin(ix) - \sum_{i=1}^3 \frac{A_i}{i} e^{-iy} \cos(ix); \quad J_1 = -\left\{ \frac{1}{4} D_1 \beta (1+y) + B_1 \right\} e^{-y} \\ J_2 &= \left[K_3 - \frac{\beta y}{384} \left\{ \text{Pe}\beta^4 \left(y^2 + \frac{3y}{2} + \frac{3}{4} \right) - \beta^2 (72 + 12\text{Pe}y + 6\text{Pe}) - 96K_1 \right\} \right] e^{-2y}. \end{aligned} \quad (C5)$$

The constants are given by $K_3 = \frac{1}{2} \left[\frac{K_1 \beta}{4} + \frac{3\beta^3}{16} + \frac{\text{Pe}\beta^3}{64} - \frac{\text{Pe}\beta^5}{512} - B_2 \right]$; $B_2 = 2\beta$.

C. Solutions for velocities

The X velocities in the inner layer have the following functional form (at this order $m = 1$):

$$\begin{aligned} \bar{U}_2 &= \bar{U}_2^{(0)} + \bar{\zeta}_0 \bar{U}_2^{(1)} + \dots; \quad \bar{U}_2^{(0)} = \beta \left[\frac{1}{2} e^{-Y} (1-Y) - \frac{3}{2} \left(Y^2 + \frac{1}{3} \right) - \frac{Y}{4} (\beta^2 + 4) \right] \cos X; \\ \bar{U}_2^{(1)} &= \sum_{i=1}^2 [G_i(Y) + m_i Y + \hat{I}_i] \sin(iX). \end{aligned} \quad (C6)$$

The constants are given by $m_1 = \frac{7}{54} \text{Pe} \beta^4 n + n\beta^2$; $m_2 = \beta^4 \left(\frac{\text{Pe}}{64} - 1 \right)$; $\hat{I}_1 = n\beta^2 \left(\frac{9\text{Pe}}{4} + \frac{3}{2} \right)$; and $\hat{I}_2 = \frac{3\beta^2}{4} \left(\frac{3\text{Pe}}{2} + 1 \right)$. The functions $G_i(Y)$ have very complicated expressions, which can be made

available (through MAPLE files) upon request to the authors. The outer layer solutions to the velocities are given by

$$\begin{aligned}
 \check{v}_2 &= \check{\zeta}_0^2 \check{u}_{\infty,2}^{(2)} \mathbf{e}_x + \nabla \times (\check{S}_2 \mathbf{e}_z); \quad \check{S}_2 = \check{S}_2^{(0)} + \check{\zeta}_0 \check{S}_2^{(1)}; \quad \check{S}_2^{(0)} = -\frac{1}{2} \beta y e^{-y} \cos(x), \\
 \check{S}_2^{(1)} &= \sum_{i=1}^2 L_i(y) \sin(ix); \quad L_1(y) = \left\{ \frac{3}{2} n \beta^2 + \left(\frac{3}{2} n \beta^2 + \hat{I}_1 \right) y \right\} e^{-y} - \frac{1}{16} D_1 \beta^2 y^2 e^{-y}, \\
 L_2(y) &= \left\{ \frac{3}{4} \beta^2 + \left(\frac{3}{2} \beta^2 + \hat{I}_2 \right) y + \left(\frac{K_1 \beta^2}{16} + \frac{7 \beta^2}{128} + \frac{\text{Pe} \beta^6}{4096} \right) y + \text{Pe} \beta^4 \left(\frac{1}{192} - \frac{\beta^2}{3072} \right) y^3 \right\} e^{-2y}, \\
 \check{u}_{\infty,2}^{(2)} &= -\beta n \left(\frac{233}{192} + \frac{11}{8} \text{Pe} \right) - n \beta^3 \left(\frac{5}{16} \text{Pe} \right) + \frac{17}{1152} \text{Pe} \beta^5 n. \tag{C7}
 \end{aligned}$$

-
- [1] R. J. Hunter, *Zeta Potential in Colloid Science: Principles and Applications* (Academic Press, New York, 1981).
- [2] D. A. Saville, Electrokinetic effects with small particles, *Annu. Rev. Fluid Mech.* **9**, 321 (1977).
- [3] P. Dutta and A. Beskok, Analytical solution of time periodic electroosmotic flows: Analogies to Stokes' second problem, *Anal. Chem.* **73**, 5097 (2001).
- [4] S. Ghosal, Lubrication theory for electro-osmotic flow in a microfluidic channel of slowly varying cross-section and wall charge, *J. Fluid Mech.* **459**, 103 (2002).
- [5] Y. Ren and D. Stein, Slip-enhanced electrokinetic energy conversion in nanofluidic channels, *Nanotechnology* **19**, 195707 (2008).
- [6] T. Nguyen, Y. Xie, L. J. de Vreede, A. van den Berg, and J. C. T. Eijkel, Highly enhanced energy conversion from the streaming current by polymer addition, *Lab Chip* **13**, 3210 (2013).
- [7] A. Revil, P. A. Pezard, and P. W. J. Glover, Streaming potential in porous media: 1. Theory of the zeta potential, *J. Geophys. Res.* **104**, 20021 (1999).
- [8] A. Revil and P. Leroy, Constitutive equations for ionic transport in porous shales, *J. Geophys. Res.* **109**, B03208 (2004).
- [9] S. Haeberle and R. Zengerle, Microfluidic platforms for lab-on-a-chip applications, *Lab Chip* **7**, 1094 (2007).
- [10] D. Mark, S. Haeberle, G. Roth, F. von Stetten, and R. Zengerle, Microfluidic lab-on-a-chip platforms: Requirements, characteristics and applications, *Chem. Soc. Rev.* **39**, 1153 (2010).
- [11] L. L. Ferrás, A. M. Afonso, M. A. Alves, J. M. Nóbrega, and F. T. Pinho, Analytical and numerical study of the electro-osmotic annular flow of viscoelastic fluids, *J. Colloid Interface Sci.* **420**, 152 (2014).
- [12] A. M. Afonso, M. A. Alves, and F. T. Pinho, Electro-osmotic flow of viscoelastic fluids in microchannels under asymmetric zeta potentials, *J. Eng. Math.* **71**, 15 (2010).
- [13] L. Fu, Analysis of electroosmotic flow with step change in zeta potential, *J. Colloid Interface Sci.* **258**, 266 (2003).
- [14] A. J. Pascall and T. M. Squires, Electrokinetics at liquid/liquid interfaces, *J. Fluid Mech.* **684**, 163 (2011).
- [15] A. Ajdari, Generation of transverse fluid currents and forces by an electric field: Electroosmosis on charge-modulated and undulated surfaces, *Phys. Rev. E* **53**, 4996 (1996).
- [16] H.-H. Wei, Shear-modulated electroosmotic flow on a patterned charged surface, *J. Colloid Interface Sci.* **284**, 742 (2005).
- [17] C.-C. Chang and R.-J. Yang, Chaotic mixing in a microchannel utilizing periodically switching electroosmotic recirculating rolls, *Phys. Rev. E* **77**, 056311 (2008).
- [18] S. S. Bahga, O. I. Vinogradova, and M. Z. Bazant, Anisotropic electro-osmotic flow over super-hydrophobic surfaces, *J. Fluid Mech.* **644**, 245 (2010).

- [19] S. Mandal, U. Ghosh, A. Bandopadhyay, and S. Chakraborty, Electro-osmosis of superimposed fluids in the presence of modulated charged surfaces in narrow confinements, *J. Fluid Mech.* **776**, 390 (2015).
- [20] E. Boyko, S. Rubin, A. D. Gat, and M. Bercovici, Flow patterning in Hele-Shaw configurations using non-uniform electro-osmotic slip flow patterning in Hele-Shaw configurations using non-uniform electro-osmotic slip, *Phys. Fluids* **27**, 102001 (2015).
- [21] E. Boyko, M. Bercovici, and A. D. Gat, Flow of power-law liquids in a Hele-Shaw cell driven by non-uniform electro-osmotic slip in the case of strong depletion, *J. Fluid Mech.* **807**, 235 (2016).
- [22] C.-K. Chen and C.-C. Cho, Electrokinetically-driven flow mixing in microchannels with wavy surface, *J. Colloid Interface Sci.* **312**, 470 (2007).
- [23] J. Zhang, G. He, and F. Liu, Electro-osmotic flow and mixing in heterogeneous microchannels, *Phys. Rev. E* **73**, 056305 (2006).
- [24] A. Ramos, A. González, A. Castellanos, N. G. Green, and H. Morgan, Pumping of liquids with ac voltages applied to asymmetric pairs of microelectrodes, *Phys. Rev. E* **67**, 056302 (2003).
- [25] A. Gonzalez, A. Ramos, N. G. Green, A. Castellanos, and H. Morgan, Fluid flow induced by nonuniform ac electric fields in electrolytes on microelectrodes. II. A linear double-layer analysis, *Phys. Rev. E* **61**, 4019 (2000).
- [26] A. Ajdari, Pumping liquids using asymmetric electrode arrays, *Phys. Rev. E* **61**, 45(R) (2000).
- [27] W. Y. Ng, S. Goh, Y. C. Lam, C. Yang, and I. Rodríguez, DC-biased AC-electroosmotic and AC-electrothermal flow mixing in microchannels, *Lab Chip* **9**, 802 (2009).
- [28] T. M. Squires and M. Z. Bazant, Induced-charge electro-osmosis, *J. Fluid Mech.* **509**, 217 (2004).
- [29] O. Schnitzer and E. Yariv, Induced-charge electro-osmosis beyond weak fields, *Phys. Rev. E* **86**, 061506 (2012).
- [30] R. V. Craster and O. K. Matar, Electrically induced pattern formation in thin leaky dielectric films, *Phys. Fluids* **17**, 32104 (2005).
- [31] E. Schaffer, T. Thurn-Albrecht, T. Russell, and U. Steiner, Electrically induced structure formation and pattern transfer, *Nature (London)* **403**, 874 (2000).
- [32] S. Dhinakaran, A. M. Afonso, M. A. Alves, and F. T. Pinho, Steady viscoelastic fluid flow between parallel plates under electro-osmotic forces: Phan-Thien-Tanner model, *J. Colloid Interface Sci.* **344**, 513 (2010).
- [33] F. H. J. van der Heyden, D. J. Bonthuis, D. Stein, C. Meyer, and C. Dekker, Power generation by pressure-driven transport of ions in nanofluidic channels, *Nano Lett.* **7**, 1022 (2007).
- [34] E. Yariv and O. Schnitzer, The electrophoretic mobility of rod-like particles, *J. Fluid Mech.* **719**, R3 (2013).
- [35] O. Schnitzer and E. Yariv, Strong-field electrophoresis, *J. Fluid Mech.* **701**, 333 (2012).
- [36] O. Schnitzer and E. Yariv, Strong electro-osmotic flows about dielectric surfaces of zero surface charge, *Phys. Rev. E* **89**, 043005 (2014).
- [37] E. Yariv, O. Schnitzer, and I. Frankel, Streaming-potential phenomena in the thin-Debye-layer limit. Part 1. General theory, *J. Fluid Mech.* **685**, 306 (2011).
- [38] M. Mao, J. D. Sherwood, and S. Ghosal, Electro-osmotic flow through a nanopore, *J. Fluid Mech.* **749**, 167 (2014).
- [39] A. S. Khair and T. M. Squires, Fundamental aspects of concentration polarization arising from nonuniform electrokinetic transport, *Phys. Fluids* **20**, 87102 (2008).
- [40] J. C. Baygents and D. A. Saville, Electrophoresis of drops and bubbles, *J. Chem. Soc. Faraday Trans.* **87**, 1883 (1991).
- [41] H. Zhao, Electro-osmotic flow over a charged superhydrophobic surface, *Phys. Rev. E* **81**, 066314 (2010).
- [42] I. Rubinstein, B. Zaltzman, and I. Lerman, Electroconvective instability in concentration polarization and nonequilibrium electro-osmotic slip, *Phys. Rev. E* **72**, 011505 (2005).
- [43] I. Rubinstein and B. Zaltzman, Electro-osmotic slip of the second kind and instability in concentration polarization at electrodialysis membranes, *Math. Model. Methods Appl. Sci.* **11**, 263 (2001).
- [44] B. Zaltzman and I. Rubinstein, Electro-osmotic slip and electroconvective instability, *J. Fluid Mech.* **579**, 173 (2007).

- [45] H. Zhao and H. H. Bau, Effect of double-layer polarization on the forces that act on a nanosized cylindrical particle in an ac electrical field, *Langmuir* **24**, 6050 (2008).
- [46] L. G. Leal, *Advanced Transport Phenomena* (Cambridge University Press, Cambridge, 2007).
- [47] U. Ghosh and S. Chakraborty, Electro-osmosis over inhomogeneously charged surfaces in presence of non-electrostatic ion-ion interactions, *Phys. Fluids* **28**, 62007 (2016).
- [48] N. Mortensen, L. Olesen, L. Belmon, and H. Bruus, Electrohydrodynamics of binary electrolytes driven by modulated surface potentials, *Phys. Rev. E* **71**, 056306 (2005).
- [49] S. S. Dukhin, Electrokinetic phenomena of the second kind and their applications, *Adv. Colloid Interface Sci.* **35**, 173 (1991).
- [50] O. Schnitzer and E. Yariv, Macroscale description of electrokinetic flows at large zeta potentials: Nonlinear surface conduction, *Phys. Rev. E* **86**, 021503 (2012).
- [51] O. Schnitzer, R. Zeyde, I. Yavneh, and E. Yariv, Weakly nonlinear electrophoresis of a highly charged colloidal particle, *Phys. Fluids* **25**, 52004 (2013).
- [52] E. Brunet and A. Ajdari, Thin double layer approximation to describe streaming current fields in complex geometries: Analytical framework and applications to microfluidics, *Phys. Rev. E* **73**, 056306 (2006).
- [53] T. J. Hughes, *The Finite Element Method: Linear Static and Dynamic Finite Element Analysis* (Dover Publications Inc., New York, 2000).
- [54] P. Deuffhard, A modified Newton method for the solution of ill-conditioned systems of nonlinear equations with application to multiple shooting, *Numer. Math.* **22**, 289 (1974).
- [55] M. Paszyński, D. Pardo, and A. Paszyńska, Parallel multi-frontal solver for p adaptive finite element modeling of multi-physics computational problems, *J. Comput. Sci.* **1**, 48 (2010).
- [56] S. Operto, J. Virieux, P. Amestoy, J.-Y. L'Excellent, L. Giraud, and H. B. H. Ali, 3D finite-difference frequency-domain modeling of visco-acoustic wave propagation using a massively parallel direct solver: A feasibility study, *Geophysics* **72**, SM195 (2007).
- [57] E. Yariv, An asymptotic derivation of the thin-Debye-layer limit for electrokinetic phenomena, *Chem. Eng. Commun.* **197**, 3 (2009).
- [58] C. M. Bender and S. A. Orszag, *Advanced Mathematical Methods for Scientists and Engineers I* (Springer, New York, 1999).
- [59] A. H. Nayfeh, *An Introduction to Perturbation Methods* (John Wiley & Sons, New York, 2011).
- [60] U. Ghosh and S. Chakraborty, Electroosmosis of viscoelastic fluids over charge modulated surfaces in narrow confinements, *Phys. Fluids* **27**, 62004 (2015).
- [61] E. Yariv, Electro-osmotic flow near a surface charge discontinuity, *J. Fluid Mech.* **521**, 181 (2004).
- [62] P. C.-H. Chan and L. G. Leal, The motion of a deformable drop in a second-order fluid, *J. Fluid Mech.* **92**, 131 (1979).
- [63] L. Højgaard Olesen, M. Z. Bazant, and H. Bruus, Strongly nonlinear dynamics of electrolytes in large ac voltages, *Phys. Rev. E* **82**, 011501 (2010).
- [64] N. G. Green, A. Ramos, A. González, H. Morgan, and A. Castellanos, Fluid flow induced by nonuniform ac electric fields in electrolytes on microelectrodes. III. Observation of streamlines and numerical simulation, *Phys. Rev. E. Stat. Nonlin. Soft Matter Phys.* **66**, 026305 (2002).
- [65] A. Ajdari, Electro-Osmosis on Inhomogeneously Charged Surfaces, *Phys. Rev. Lett.* **75**, 755 (1995).
- [66] M. S. Kilic, M. Z. Bazant, and A. Ajdari, Steric effects in the dynamics of electrolytes at large applied voltages. I. Double-layer charging, *Phys. Rev. E* **75**, 021502 (2007).
- [67] S. S. Dukhin and V. N. Shilov, Theory of static polarization of diffuse part of thin electric double layer of spherical particles, *Colloid J. USSR* **31**, 564 (1969).
- [68] V. N. Shilov and S. S. Dukhin, Theory of polarization of diffuse part of a thin double layer at a spherical particle in an alternating electric field, *Colloid J. USSR* **32**, 90 (1970).
- [69] K. T. Chu and M. Z. Bazant, Nonlinear electrochemical relaxation around conductors, *Phys. Rev. E* **74**, 011501 (2006).
- [70] U. Ghosh and S. Chakraborty, Patterned-wettability-induced alteration of electro-osmosis over charge-modulated surfaces in narrow confinements, *Phys. Rev. E* **85**, 046304 (2012).